Department of Physics and Astronomy
Ruprecht-Karls-Universität Heidelberg

Master Thesis in Physics
submitted by

Anton Eberhardt

born in Heidenheim a. d. Brenz, Germany

2024

Advances in construction of a ^{23}Na-^{39}K Ultracold Bosonic Mixture Experiment for Analog Quantum Simulations

This Master Thesis has been carried out by Anton Eberhardt at the
Kirchhoff Institute for Physics in Heidelberg
under the supervision of
Prof. Dr. Markus Oberthaler

ABSTRACT

Advances in construction of a ^{23}Na-^{39}K Ultracold Bosonic Mixture Experiment for Analog Quantum Simulations

In this thesis, I present the progress made in the construction of a novel $^{23}\mathrm{Na}$-$^{39}\mathrm{K}$ ultracold bosonic mixture experiment. By precisely tuning intra- and inter-species interactions, this system can serve as an experimental platform for analog quantum simulations. The main focus of this work is on the optimization of the laser cooling sequence used to achieve quantum degeneracy for sodium, with the goal of realizing dual species quantum degeneracy in the future. I start with an overview of the experimental setup, discussing in particular the performance of the sodium oven, the characterization of a tapered amplifier module used for amplification of laser light for potassium and optimization procedures for the atom sources. I also detail investigations to improve the magnetic quadrupole trap, as well as improvements to the high resolution absorption imaging system. Additionally, I discuss the decision to replace the magnetic trap with grey molasses cooling for sodium and the modifications to the laser system this transition required.

Fortschritte beim Aufbau eines ^{23}Na-^{39}K-Experimenents für Analoge Quantensimulationen in Ultrakalten Bosonischen Mischungen

In dieser Arbeit präsentiere ich die Fortschritte im Aufbau eines neuen $^{23}\mathrm{Na}$-$^{39}\mathrm{K}$ Experiments für ultrakalte bosonische Mischungen. Durch genaue Kontrolle sowohl über Wechselwirkungen zwischen Teilchen der selben Atomsorte als auch zwischen Teilchen verschiedener Atomsorten stellt dieses System eine experimentelle Plattform für analoge quantum Simulationen dar. Der Fokus dieser Arbeit liegt auf der Verbesserung der Laserkühlsequenz, die das Erzeugen eines Natrium Bose-Einstein-Kondensats ermöglicht, mit dem Ziel zukünftig ein Dualspezies-Kondensat herstellen zu können. Ich beginne mit einer Zusammenfassung des experimentallen Aufbaus, wobei insbesondere die Funktionalität des Natrium-Ofens, die Charakterisierung eines "tapered amplifier" Moduls zur Verstärkung von Laserlicht für Kalium und Optimisierungsverfahren für die Atomquellen diskutiert werden. Weiterhin beschreibe ich Untersuchungen zur Verbesserung der magnetischen Quadrupolfalle und des hochauflösenden Bildgebungsystems. Anschließend diskutiere ich unsere Entscheidung, die magnetische Quadrupolfalle durch die Anwendung der "grey molasses" Kühltechnik für Natrium zu ersetzen und die nötigen Veränderungen unseres Lasersystems die mit diesem Schritt einhergehen.

CONTENTS

1 Introduction 1
  1.1 Bose-Einstein-Condensation 1
  1.2 Miscibility of a Binary Bose-Einstein-Condensate 3
  1.3 Overview of the thesis 4
2 Tools and Techniques for Laser Cooling 7
  2.1 Magneto-Optical-Trap (MOT) 7
  2.2 Dark Spontneous-force Optical Trap (dark SPOT) 8
  2.3 Grey Molasses 9
  2.4 Temperature measurements by ballistic expansion . . . 12
3 Overview of the Experiment 13
  3.1 Laser tables 13
    3.1.1 Current Laser Systems and Frequency Stabilization 13
    3.1.2 Frequency shifting 15
    3.1.3 Changes to implement sodium D_1 light 16
    3.1.4 Light Amplification for Potassium 18
    3.1.5 2D MOT TA characterization 22
  3.2 Vacuum System and Atom Sources 27
    3.2.1 Two dimensional Magneto-Optical-Traps (2D MOT) 27
    3.2.2 Optimizing the 2D MOTs 29
    3.2.3 Sodium Oven Issues 31
  3.3 Absorption Imaging Systems 34
4 Optimization of the Cooling Sequence 39
  4.1 Previous Sequence 39
  4.2 Challenges involving the magnetic trap 40
    4.2.1 Sloshing in the magnetic trap 43
    4.2.2 Offset Coil Calibration 46
    4.2.3 Upgrade of the power supplies for the offset coils 47
  4.3 Optimizing the crossed Optical Dipole Trap (cODT) . . . 49
    4.3.1 Dipole laser setup 49
    4.3.2 Asymmetry of the Dipole beams 51
  4.4 Our Cooling Sequence: Then and now. 55
    4.4.1 Adding Potassium 55
    4.4.2 Sodium Grey Molasses 56
    4.4.3 Re-optimization of Potassium 57
    4.4.4 Potassium Grey Molasses 58
    4.4.5 Dual Species Operation 60
5 Outlook and Conclusion 63
  5.1 What the future holds 63
  5.2 Conclusion 64
Appendices 65
A Bidirectional Power Supply 67
List of Acronyms 69

List of Figures 77
Acknowledgments 85

1

INTRODUCTION

In the past 40 years the research field around ultra cold atoms has matured a lot and today's scientists are able to exert an astounding amount of precision in the control of cold atom samples and Bose-Einstein-Condensates (BECs). By carefully tuning the potential landscape and the interactions between particles in the sample, in principle it is now possible to simulate a wide range of interesting quantum systems spanning topics like condensed matter and high energy physics [27], and even cosmology [48]. Such systems are hard to measure or completely inaccessible with conventional methods, thus, the interest in *analog quantum simulators* has grown substantially over the last few years[1].

Within the realm of analog quantum simulators, ultra cold quantum mixture experiments offer a platform to investigate unique types of problems that can't be studied using a single component quantum gas, e.g. miscible-immiscible phase transitions in binary BEC-mixtures [3, 45, 46] or how BECs behave with impurities present [40].

The SoPa experiment is a project set out to investigate such exciting new fields, as the Na-K system promises rich possibilities with many individual tuning knobs to generate novel systems. In particular, the rich spectrum of Feshbach Resonances [6] for this combination [38] represent a powerful tool for precisely manipulating the character of our many-body-system.

In this chapter I want give a small intro on the theory of BECs, why $^{23}\mathrm{Na}$ and $^{39}\mathrm{K}$ were chosen for this experiment and finally I will present a specific example of a physical system that could be investigated in the future using SoPa[2]. The chapter will conclude with an outline for the rest of this thesis.

1.1 BOSE-EINSTEIN-CONDENSATION

The phenomenon of Bose-Einstein-Condensation was first proposed by Einstein following Bose's description of Planck's black body radiation by the means of statistical mechanics in the early 20th century [28]. It took over 7 decades until this exotic state of matter could be observed experimentally in dilute atomic gases[3], which represents the inception of ultra-cold-atom research as we know it today. For a BEC to form, the particles of the system need to be bosonic, meaning they posses integer spin and therefore follow the Bose-Einstein-quantum statistics given by

---

[1] A broad overview of the possible uses for these experiments is given in the reviews [4, 13].

[2] This section will be a concise summary of the introduction from [24].

[3] Rubidium by C. Wieman and E. Cornell et al. [1] and sodium by W. Ketterle et al. [10]

$$N(E) = \frac{1}{e^{\beta(E-\mu)} - 1} \tag{1}$$

where $N(E)$ is the occupation number of a quantum state with energy E, $\beta = 1/k_B T$ and μ represents the chemical potential [28]. For sufficiently low temperatures, the occupation number of ground state increases dramatically. Generally, a BEC is defined as a state of the system, where the ground state is macroscopically occupied. In a three dimensional cloud of massive particles, this phase-transition happens at a Phase Space Density (PSD) of

$$n\lambda_{th}^3 = 2.612... \tag{2}$$

where λ_{th} is the thermal de Broglie wavelength $\lambda_{th} = \sqrt{2\pi\hbar^2/mk_B T}$ and n represents the number density of particles (see e.g. [30] for more details).

Treating a BEC of interacting particles in the mean field approximation, the interaction strength is proportional to the density of particles, which is given by the magnitude of the macroscopic wavefunction $|\Psi(\vec{r},t)|^2$. Together with the conventional terms for kinetic and potential energy, this yields a non-linear Hamiltonian know as the *Gross-Pitaevskii-equation* [14, 32]:

$$i\hbar\Psi(\vec{r},t) = \left[-\frac{\hbar^2}{2m}\nabla^2 + V(\vec{r}) + g|\Psi(\vec{r},t)|^2 \right] \Psi(\vec{r},t). \tag{3}$$

The density dependent term representing the interactions between particles is scaled by the coupling strength $g = 4\pi\hbar^2 a/m$, with a being the s-wave scattering length. One way to approximately solve this system and describe its collective behavior is *Bogoliubov theory* [5], a thorough derivation of which can be found in various books on the topic (see e.g. [30, 31]). Here, only the resulting dispersion relation

$$\epsilon(p) = \left[\frac{gn}{m} p^2 + (\frac{p^2}{2m})^2 \right]^{1/2} \tag{4}$$

for elementary excitations will be of interest to us, since it relates to the maximal domain size of the two phases in demixing experiments, which will be the topic of the following section.

1.2 MISCIBILITY OF A BINARY BOSE-EINSTEIN-CONDENSATE

In this section, I will give a qualitative explanation of one physical phenomenon, the demixing of a binary BEC mixture, which we plan to observe in the near future. A large part of the theoretical fundamentals will be omitted, since they are not relevant for the rest of this thesis. Rather, this section should be viewed as a glimpse on what is possible and a motivation on why this system is worth investigating. For general details on miscibility, refer to [26, 39] and their references, for information on miscibility in a $^{23}\mathrm{Na}$-$^{39}\mathrm{K}$-system, see [15].

With a two component BEC, one has to not only account for the interactions within each component, but also for interactions between particles of different components. Therefore, three parameters representing the coupling strengths are required to accurately describe the system:

$$g_{11} = \frac{4\pi\hbar^2 a_{11}}{m_1}, g_{22} = \frac{4\pi\hbar^2 a_{22}}{m_2}, g_{12} = \frac{4\pi\hbar^2 a_{12}}{m_r}, \tag{5}$$

where g_{ii} (and likewise the scattering length a_{ii}) represents interactions between particles of equal type (*intraspecies* interactions) and g_{12} represents interactions between particles of different type (*interspecies* interactions) with the reduced mass $m_r = m_1 m_2/(m_1 + m_2)$. The Hamiltonian for each component is analogous to Equation 3, but with an additional density dependent term coming from the other component in the mixture, resulting in two couple Gross-Pitaevskii-equations:

$$i\hbar\Psi_1(\vec{r},t) = \left[-\frac{\hbar^2}{2m}\nabla^2 + V_1(\vec{r}) + g_{11}|\Psi_1(\vec{r},t)|^2 + g_{12}|\Psi_2(\vec{r},t)|^2\right]\Psi_1(\vec{r},t) \tag{6}$$

$$i\hbar\Psi_2(\vec{r},t) = \left[-\frac{\hbar^2}{2m}\nabla^2 + V_2(\vec{r}) + g_{22}|\Psi_2(\vec{r},t)|^2 + g_{12}|\Psi_1(\vec{r},t)|^2\right]\Psi_2(\vec{r},t). \tag{7}$$

Using these equations, one can derive a condition for the *miscibility* of the system, i.e. if it is energetically more favorable to form a homogeneous mixture or to exhibit two spacially separated phases. This condition is characterized by the miscibility parameter:

$$\delta_g = \frac{g_{12}^2}{g_{11}g_{22}} - 1, \tag{8}$$

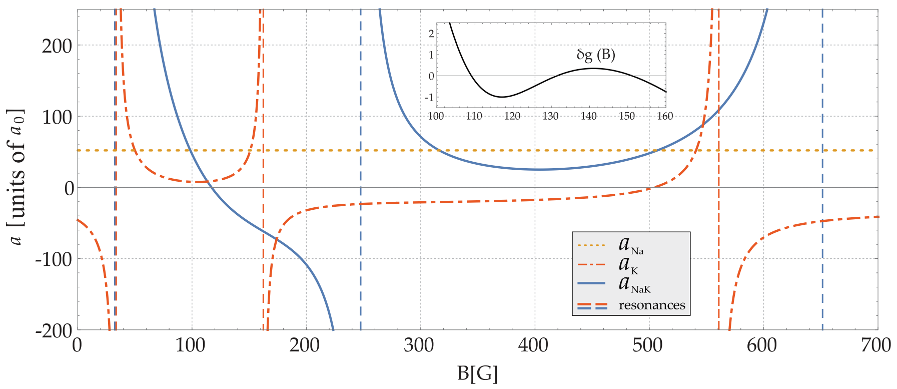

Figure 1.1: Scattering lengths of $^{23}\mathrm{Na}$ and $^{39}\mathrm{K}$ (a_{Na} and a_K respectively) and interspecies scattering length (a_{NaK}) as a function of bias field strength (both species are in the $|F = 1, m_f = -1\rangle$ state.). The relation between scattering length and coupling strength is given in Equation 5. The miscibility parameter $\delta_g(B)$ is plotted in the inset. Figure taken from [38].

which is defined such that a miscible system will have $\delta_g < 0$. Note that this depends only on the different parameters for the coupling strength, which we have seen before. These parameters can be tuned by utilizing the aforementioned Feshbach-resonances by applying a constant magnetic field and varying its magnitude. The $^{23}\mathrm{Na}$-$^{39}\mathrm{K}$-system exhibits a large amount of usable intra- and interspecies Feshbach-resonances [38], which are summarized in Figure 1.1. The inset of this figure also visualizes that different miscibility regimes are easily accessible with relatively small magnetic fields.

It is interesting to consider the temporal behavior of this system after quenching the miscibility parameter from miscible to immiscible. One can calculate a dispersion relation for collective excitations similar to Equation 4, which can be used to predict the scaling behavior of the domain formation and the maximal domain size in equilibrium [24, 39], which we would be able to observe with our experiment.

There are two reason why we deem it interesting to investigate this topic: For one, by measuring the demixing behavior of a real system, one could verify numerical simulations like [39]. On the other hand, the way towards performing this measurement will serve as an opportunity to increase our understanding of all the experimental details specific to the SoPa and the manipulation of a $^{23}\mathrm{Na}$-$^{39}\mathrm{K}$-system, which will result in valuable lessons for future, more complex endeavors.

1.3 OVERVIEW OF THE THESIS

After this short motivation of the physics perspective of the SoPa, I will continue with Chapter 2 by explaining some of the important laser cooling principles and techniques that are employed in our experiment and are relevant for this thesis. Afterwards, I will outline the general design of the project in Chapter 3, focusing on topics and parts of the experiment that are not explicitly part of the cooling sequence used for producing a BEC, like e.g. the laser systems and the atom sources. Finally, in Chapter 4 I will describe both the previous and the new approach to our cooling sequence, focusing on some of the individual steps within that sequence and the efforts that have been made to improve them. The thesis will conclude with an outlook on two large projects that will be implemented in the near future.

2

TOOLS AND TECHNIQUES FOR LASER COOLING

Here, I want to give a quick overview of the working principles behind some of the laser cooling techniques that will be the topic of later chapters. Since this subject has been covered extensively in literature (e.g. [12, 28, 41]), the following will be kept brief. For a more detailed description, the reader can refer to the literature referenced throughout this section.

2.1 MAGNETO-OPTICAL-TRAP (MOT)

The Magneto Optical Trap (MOT) (first demonstrated by [35]) represents the basis for most cold atom experiments running today, since it is a well established way to trap a large number of atoms while also cooling them down to sub-milli-Kelvin temperatures.

It utilizes a pair of counter-propagating laser beams for each of the three directions of a Cartesian coordinate system, all meeting in the same point. All beams have the same frequency, which is slightly below the resonant frequency of a suitable transition (we assume a two-level atom for now). Due to the Doppler effect, every moving atom in the center of the trap will be shifted closer to resonance with least one of the 6 beams due to its velocity component in this direction. Since the absorption introduces a momentum kick along the beam direction and the following spontaneous emission (and the associated momentum kick) does not have a preferred direction, this results in an average scattering force acting on the atom, which points exactly into the opposite direction of the atoms velocity[1]. When using circularly polarized light and adding a magnetic quadrupole field (which can be generated by two coils in anti-Helmholtz configuration), one can introduce a position dependent term to this scattering force, since the atoms are not only shifted into resonance by their velocity, but also by the position dependent shift of the Zeeman levels arising from the magnetic field gradient. Figure 2.1 illustrates the configuration of beams (for simplicity only in z-direction) that leads to a position dependent force pointing towards $z = 0$: At $z < 0$, the $\Delta M_j = +1$ transition is shifted closer to resonance, making the absorption of σ^+-light propagating in positive z direction more likely. For positive values of z, the situation is the exact opposite, with the $\Delta M_j = -1$ being closer to resonance, therefore preferably σ^- light coming from the right is absorbed.

---

[1] Since this force is analogous to an object moving through a viscous fluid, this technique is called "optical molasses cooling" [7].

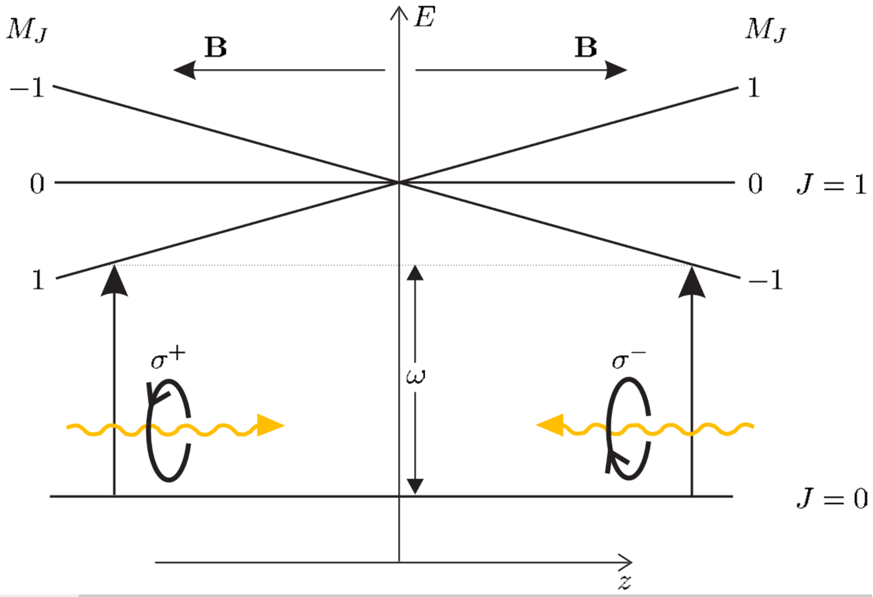

Figure 2.1: One dimensional schematic illustration of the mechanism of a MOT. The B-field switches directions at $z = 0$ and the counter-propagating MOT-beams with the frequency of $f = \omega/2\pi$ have opposite circular polarization. This results in a force pointing towards the center of the coordinate system, because of the position dependent energy of different M_J states. Figure adapted from [12].

2.2 DARK SPONTNEOUS-FORCE OPTICAL TRAP (DARK SPOT)

The dark Spontaneous-force Optical Trap (SPOT) (first demonstrated by [22]) is a variation of a regular MOT, which can significantly increase the density inside the trap by a factor of ≈ 100. The number of trapped atoms in a MOT is limited mainly by two processes, which the are both suppressed in a dark SPOT-setup: The first is a repulsive force resulting from atoms reabsorbing photons from the spontaneous emissions by other atoms in the cloud instead of photons from the laser beams. This leads to an outward pressure which increases with density until a balance with the scattering force is reached [22]. In the second process, excited state atoms collide with ground state atoms, resulting in a trap loss since some of the excitation energy is converted to kinetic energy [22, 33].

Technically, both these processes do not depend the *density of atoms*, but rather on the *density of excited state atoms*. If one considers a three level atom instead of a two level atom, it would be possible to have most atoms in the trap populate the third state, which is also called "dark" state, as it is not interacting with the MOT-beams. Without these interactions however, there is also no trapping force containing the atoms inside the trap, as well as no cooling effect from the moment they enter the dark state.

This issue can be overcome by creating a region that operates like a regular MOT, which completely encloses a region where the atoms preferably populate the dark state (a "dark spot" inside the MOT, so to say), thus avoiding the above mentioned limitations on density. In practice, we can achieve this by employing two more beams with a relative angle of approx. 90° aimed at a regular MOT, but the middle of each beam is blocked, so they exhibit a "donut"-shape. This leaves a region in the middle of trap, where their light does not reach. The frequency of these two beams has to be such that it pumps the dark state atoms back into the "cooling cycle" (excitation and spontaneous emission between "bright" state and excited state), where they again experience the regular scattering force produced by a MOT until they fall back to the dark state[2].

2.3 GREY MOLASSES

The laser cooling schemes above are great for trapping and cooling high number of atoms, however there are fundamental limits on the reachable temperatures, which have been discussed extensively in literature (e.g. the *Doppler cooling limit*, see [12, 41]). More elaborate optical cooling schemes can be used to reach temperatures far below the Doppler limit, one of which is the so called *grey molasses cooling*, which can be applied to a λ-type system with two ground states $|g_1\rangle$ and $|g_2\rangle$ and one excited state $|e\rangle$ (see Figure 2.2). Here, we can make use of a Raman-transitions between the two ground states, which can be excited by irradiating the system with two frequencies of light, $\omega_1 = \omega_{g_1 \to e} + \Delta + \delta$ and $\omega_2 = \omega_{g_2 \to e} + \Delta$ [12], where $\delta = 0$ represents the resonant case[3]. One can represent the resulting atom-light-system in the dressed state picture, the three energy eigenstates of which are called excited state $|e'\rangle$, bright state $|b\rangle$ and dark state $|d\rangle$, since the dark states transition probability to the excited state is negligibly small while the bright states couples to the excited state rather strongly [51]. Additionally, the dark and bright states are coupled via a velocity dependent term (*motional coupling*), which makes it possible to pump slow atoms to the dark state: atoms in the bright state continue to scatter photons, resulting in a random walk in velocity space with the step size $\hbar k$, where k is the wavevector of the absorbed or emitted photon. At each spontaneous emission, there is a chance for the atom to enter the dark state. However, it will only stay in the dark state if its velocity is sufficiently small, otherwise it will reenter the bright state through the motional coupling, where it continues its random walk. Through this process, which is referred to as Velocity-selective Coherent Population Trapping (VSCPT) [2], slow atoms will eventually accumulate in the dark state.

---

[2] For this to work properly, the amount of scattering events in the cooling cycle should be $\gg 1$, i.e. the probability of entering the dark state after a scattering event should be small.

[3] Since this is a two-photon transition, Δ can be $\neq 0$ and one could still observe a resonance feature. Therefore, Δ is usually chosen relatively large (e.g. $\approx 10\Gamma$ for sodium [8], where Γ denotes the linewidth of the transition), such that unwanted single photon excitations are suppressed.

For grey molasses cooling, the mechanism above is combined with a cooling force, accelerating the accumulation in the dark state. This is achieved by exploiting the energy dependence of the bright state with respect to polarization, which arises when choosing Zeeman sub levels of $m_f = -1$, $m_f = 0$, $m_f = +1$ for $|g_1\rangle$, $|e\rangle$ and $|g_2\rangle$ respectively [9, 51]. The polarization can be spacially modulated e.g. by using two counter propagating beams with perpendicular linear polarization ("lin $\perp$ lin"-configuration[4]). Here it is useful to note that the energy difference between the dark and bright state can be adjusted by the choice of the detuning Δ. For the purpose of grey molasses cooling, the light should be blue-detuned, in which case the energy of the dark state is lower than the that of the bright state. The situation is depicted at the bottom of Figure 2.2: We have the bright state with its polarization dependent energy above the constant energy dark state. The probability of an atom being transferred from the dark to the bright state is largest where the two states are closest together, i.e. in the potential minimum of the bright state [47]. From here, any atom with velocity will convert some of its kinetic energy to potential energy by "climbing the hill". The potential energy gained by the atom can be irradiated during the next scattering event, removing it from the system. Furthermore, the probability of a scattering event is highest at the potential maximum of the polarization gradient, maximizing the amount of potential energy gained. With each spontaneous emission, the atoms may decay to the dark state, again resulting in a statistical accumulation of slow atoms in the dark state, as we have seen before, while kinetic energy is actively removed from the system with each cycle.

In reality, atoms will not exhibit a perfect 3-level system, instead one needs to account for all possible electronic states. This causes the "dark" state of the dressed state picture to not be perfectly dark, therefore scattering some amount photons, hence the name "grey" molasses (since its a "grey" state instead of a "dark" state). In alkali atoms, one can usually find configurations, for which the scattering rate in the grey state is low enough to still facilitate efficient cooling.

---

[4] For this configuration it is fairly easy to understand how the polarization gradient is formed, since it can be visualized as a superposition of two perpendicular harmonic oscillators, whose phase difference depends on the position in space. In practice, we use circularly polarized light with opposite directions σ^+ and σ^-.

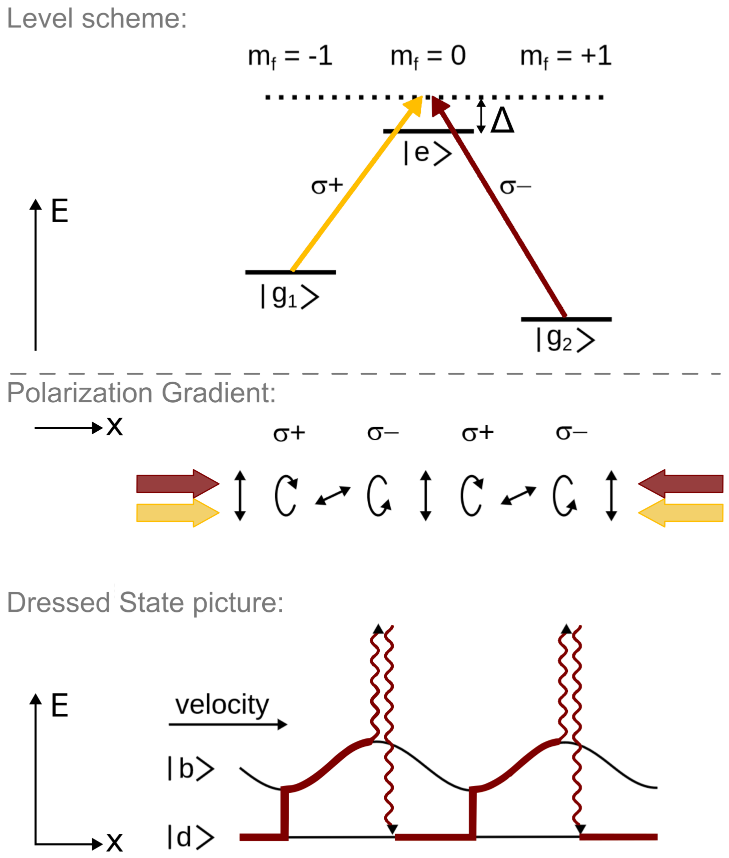
Level scheme:
m_f = -1
m_f = 0
m_f = +1
Δ
|e>
σ+
σ−
E
|g₁>
|g₂>
Polarization Gradient:
x
σ+
σ−
σ+
σ−
Dressed State picture:
E
velocity
|b>
|d>
x

Figure 2.2: Illustration of the grey molasses cooling mechanism. (Upper panel) The level scheme of the λ-type system is plotted with the two required laser frequencies in Raman-condition and the detuning Δ. (Lower Panel) The system is simultaneously irradiated with two counter-propagating beams containing both aforementioned frequencies. Their polarizations are in "lin $\perp$ lin"-configuration, resulting in a polarization gradient. This gradient gives rise to a position-dependent energy of the bright state $|b\rangle$ in the dressed state picture, while the dark state $|d\rangle$ stays unmodulated. The probability of atoms in the dark state coupling to the bright state is highest in the potential minimum. The movement of the atom causes it to convert kinetic energy to potential energy ("climbing the hill") before being excited and falling back down to the dark state. Figure adapted from [47].

2.4 TEMPERATURE MEASUREMENTS BY BALLISTIC EXPANSION

Before reaching quantum degeneracy, the velocity distribution of the trapped atoms will be a Maxwell-Boltzmann-distribution. If the density distribution of atoms inside the trap is also known, one can derive how the cloud would expand in free space once all the trapping forces are switched off. Assuming a Gaussian as initial distribution this leads to the formula

$$\sigma^2(t) = \sigma^2(t=0) + \frac{k_B T}{m} t^2 \tag{9}$$

for the width σ of the cloud [49]. By measuring the density distribution at different Time Of Flights (TOFs)[5], we can estimate the temperature of the cloud, which is crucial for validating the functionality of the employed cooling schemes.

---

[5] TOF is defined as the time between switching of all trapping and cooling forces and the point in time at which we measure the cloud, i.e. "take a picture" (see Section 3.3).

3

OVERVIEW OF THE EXPERIMENT

In this chapter, I will outline some of the challenges we have faced with different parts of the experiment over the past year, while also giving a broad overview of the overall design of the project, including specifics on the stabilization, frequency shifting and amplification of laser light for both species, the vacuum system and the atom sources.

3.1 LASER TABLES

The various laser cooling techniques described in the previous chapter require a sizable collection of different laser beams and careful control of their properties. Figure 3.1 depicts the level schemes for $^{23}\mathrm{Na}$ and $^{39}\mathrm{K}$ as well as the transitions we need to address for our cooling sequence. The MOTs of our experiments are operated with red-detuned light on the D_2-line for both species, driving $|F=2\rangle \to |F'=3\rangle$ transitions ("cooling" transition). While we assumed an ideal two level system before, in practice this is not accurate, since off-resonant $|F=2\rangle \to |F'=2\rangle$ transitions are possible, which can relax back to the $|F=1\rangle$ ground state. This state is not addressed by the cooling light, so another beam tuned to the $|F=1\rangle \to |F'=2\rangle$ transition ("repump" transition) is required to close the optical cycle in good approximation. For sodium, the $|F=1\rangle$-state is utilized as the dark state of the dark SPOT explained in Section 2.2.

For the grey molasses cooling, which we utilize for potassium and recently also implemented for sodium (see Section 4.4), we additionally need light on the D_1-line. While all required frequencies near the D_2-line can efficiently be generated by splitting and frequency-shifting the beam of a single laser using well established technologies[1], the frequency difference between D_1 and D_2 is too large (around $1.5\mathrm{THz}$ for potassium and $0.5\mathrm{THz}$ for sodium), necessitating additional laser sources, which will be described in the following section together with the technique used to stabilize them to the desired frequencies.

3.1.1 *Current Laser Systems and Frequency Stabilization*

For sodium, we use a *TOPTICA Photonics TA-SHG-Pro* with an output of around $1.3\mathrm{W}$ for the D_1-light and a frequency doubled fiber laser to generate roughly $4\mathrm{W}$ of D_2-light. The fiber laser uses a $1178\mathrm{nm}$ *Toptica DLC-Pro* as seed laser and a *MPB-YFL-P-Series* ytterbium laser as pump laser. This MPB system also contains a non-linear crystal

---

[1] see Section 3.1.2

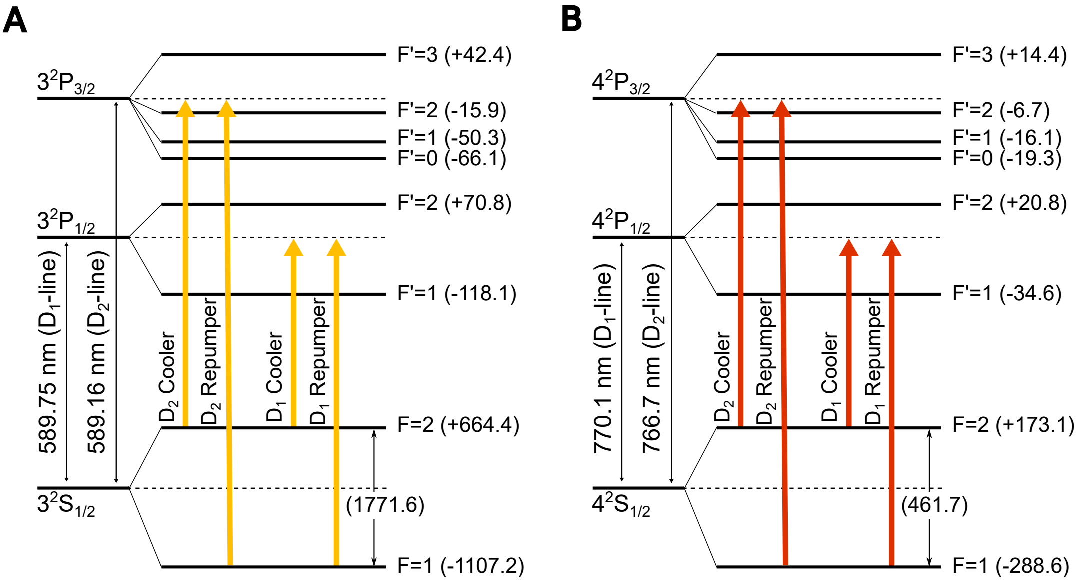
A
3²P3/2
F'=3 (+42.4)
F'=2 (-15.9)
F'=1 (-50.3)
F'=0 (-66.1)
3²P1/2
F'=2 (+70.8)
F'=1 (-118.1)
589.75 nm (D1-line)
589.16 nm (D2-line)
D2 Cooler
D2 Repumper
D1 Cooler
D1 Repumper
F=2 (+664.4)
3²S1/2
(1771.6)
F=1 (-1107.2)
B
4²P3/2
F'=3 (+14.4)
F'=2 (-6.7)
F'=1 (-16.1)
F'=0 (-19.3)
4²P1/2
F'=2 (+20.8)
F'=1 (-34.6)
770.1 nm (D1-line)
766.7 nm (D2-line)
D2 Cooler
D2 Repumper
D1 Cooler
D1 Repumper
F=2 (+173.1)
4²S1/2
(461.7)
F=1 (-288.6)

Figure 3.1: Energy level schemes for the atoms used in our experiment (A: ^{23}Na, B: ^{39}K). The transitions utilized in our cooling sequence are denoted by colored arrows, the frequency shifts from the hyperfine structure are written in brackets in units of MHz (distances are not to scale). The values for sodium were taken from [42], the potassium values from [43]. The figure itself was largely adapted from [24].

for doubling the frequency of the light after it has been amplified. For Potassium, one unit of the model *Toptica DLC-Pro* is used for each D_1 and D_2, both supplying around $25\mathrm{mW}$ of power. Regarding the sodium light, the power output suffices for our experiment, the potassium light however needs to be further amplified, which we achieve by utilizing multiple Tapered Amplifier (TA) diodes, which will be the topic of Section 3.1.4.

Besides supplying enough power, it is also crucial that the lasers are stable in frequency. For this, we lock them to a atomic reference with *Saturated Absorption Spectroscopy* [34] in conjunction with *Zeeman Modulation Locking* [52]. In this scheme, we generate the error signal used for locking by coupling some of the light into a spectroscopy cell containing the respective element. This beam is then reflected back through the cell and measured by a photodiode on the other end, measuring the intensity of the beam after passing through the cell two times (i.e. the spectroscopy signal). Furthermore, the spectroscopy cells are wrapped in copper wire, which is supplied by a sinusoidally modulated current. If the light entering the spectroscopy cell has circular polarization, the amount of light that is absorbed depends on the B-field present in the system due to the shift of the Zeeman levels. This makes it possible to generate an error signal by utilizing a lock-in amplifier.
The sodium D_2 laser is locked on the center of peak corresponding to

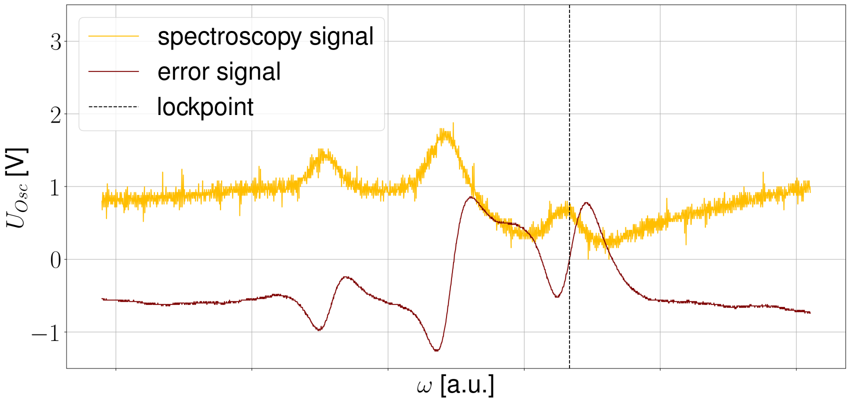

Figure 3.2: Spectroscopy signal from saturated absorption spectroscopy registered by the photodiode for the D_1 lock and the error signal generated from it. The lockpoint is marked by a dashed line. The data was taken using an oscilloscope. The spectroscopy signal was shifted downward by $0.33\mathrm{V}$ and then scaled by a factor of 50 to improve its visibility in this plot. The visible peaks correspond to the following transitions (from left to right): $|F = 2\rangle \rightarrow |F' = 2\rangle$, $|F = 2\rangle \rightarrow |F' = 1, 2\rangle$ (CO) and $|F = 2\rangle \rightarrow |F' = 1\rangle$.

the transitions from $|F = 2\rangle$ to $|F' = 2\rangle$, the $|F' = 2, 3\rangle$ crossover (CO) and to $|F' = 3\rangle$. The lockpoint of the sodium D_1 laser is the $|F = 2\rangle \rightarrow |F' = 1\rangle$ transition. The potassium D_1 and D_2 lasers are both locked to their respective ground state crossover dips of the spectroscopy signals[2].

For more specifics on our sodium D_2 and potassium D_1 and D_2 laser locks, refer to [24]. Figure 3.2 contains details on the sodium D_1 lock, which is plotted here since it has only been added to our system quite recently (see Section 3.1.3). It is worth mentioning that we use the same spectroscopy cell to lock both lasers, which is illustrated in Figure 3.3 for sodium. The potassium spectroscopy is operated in an analogous configuration. Lastly, note that the sodium D_2 laser is not locked exactly on the resonance frequency, since an offset is introduced by an Acousto Optical Modulator (AOM) double pass before coupling light into the spectroscopy cell (see also Figure 3.5).

3.1.2 *Frequency shifting*

The arrows in Figure 3.1 represent the most important frequencies for operating a MOT and performing grey molasses cooling, however, in practice we also need additional, slightly different frequencies for vari-

---

[2] For D_2, the individual CO-peaks are too broad to be resolved separately, resulting in one large resonant feature we can lock on. For D_1, we lock on the $|F = 1, 2\rangle \rightarrow |F' = 2\rangle$ CO transition. Through the locking electronics, the lock point is shifted an additional $-20\mathrm{MHz}$ for D_2 and $+13.9\mathrm{MHz}$ for D_1.

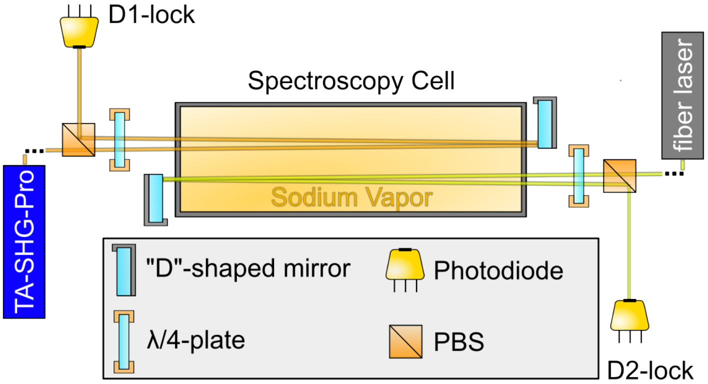

Figure 3.3: Schematic illustration of the sodium spectroscopy setup. Both beams enter the spectroscopy cell in opposite directions and are retroreflected by "D"-shaped mirrors to not obstruct the respective other beam. A Polarizing Beam Splitter (PBS) together with a $\lambda/4$-plate is used to guide the beam onto a fast photodiode after passing the cell twice.

ous purposes. A summary of all optical paths is given in Table 3.1 for sodium and in Table 3.3 for potassium. Most frequencies are generated using AOMs in double pass configuration, with the exception of the repumper light for sodium on both the D_1 and the D_2 line, since the frequency shift of roughly 1.7GHz is too large to be efficiently generated by an AOM double pass. For the D_1-repumper and the D_2-repumping light for the 2D-MOT (both the MOT beams and the slower beam), this shift is generated by Electro Optic Modulators (EOMs), which introduce symmetric frequency sidebands with a tuneable offset to the carrier frequency.

Since the dark SPOT-repumper enters the science chamber seperate from the cooling light it is important that it doesn't contain a component of cooling light itself to not unnecessarily alter the trap geometry. Likewise, we do not want to have any cooling light present in the repumper used for imaging, making an EOM not suitable for these applications. Instead, the repumping light is generated using an AOM in quadruple pass configuration, which is illustrated in Figure 3.4.

3.1.3 *Changes to implement sodium D_1 light*

As we will see later in this thesis (Section 4.4), we drastically altered our cooling sequence to adapt to challenges we have encountered with the previous approach. Specifically, we wanted to utilize D_1 grey molasses cooling not only for potassium, but also for sodium, which has already been demonstrated by Colzi et al. [8] and can reach temperatures as low as $9\mu\text{K}$. This necessitated a restructuring of our laser system: Previously, we used two units of the aforementioned *TOPTICA Photonics TA-SHG-Pro* in "leader-follower-configuration" (described in detail in [24]). In this setup, the follower was used only for supplying the slower

	Transition $\|F\rangle \rightarrow \|F'\rangle$	Detuning $[\mathrm{MHz}]$	AOM/EOM frequency $[\mathrm{MHz}]$
D_2 Spectroscopy Offset	$\|2\rangle \rightarrow \|2,3\rangle$ CO	+176	+88
2D MOT cooler	$\|2\rangle \rightarrow \|3\rangle$	-37	-93
2D MOT repumper	$\|1\rangle \rightarrow \|2\rangle$	-55	1695.6
Slower cooler	$\|2\rangle \rightarrow \|3\rangle$	-73	-111
Slower repumper	$\|1\rangle \rightarrow \|2\rangle$	-71	1715.6
Push	$\|2\rangle \rightarrow \|3\rangle$	+1	-73
3D MOT cooler	$\|2\rangle \rightarrow \|3\rangle$	-8	-78
3D MOT repumper	$\|1\rangle \rightarrow \|2\rangle$	-11	-389
Imaging	$\|2\rangle \rightarrow \|3\rangle$	0	-88
D_1 cooler	$\|2\rangle \rightarrow \|2\rangle$	+99	+144
D_1 repumper	$\|1\rangle \rightarrow \|2\rangle$	+99	1771.6

Table 3.1: Current configuration of detunings with the respective AOM and EOM frequencies for $^{23}\mathrm{Na}$. If an AOM frequency is denoted as a negative number it means that the first negative order is used. Every frequency shift is realized using an AOM double pass setup except the 3D MOT repumper (quadruple pass) and the repumper for the 2D MOT, the slower and the D_1 grey molasses (EOMs). For entries noted with D_1, $3^2P_{1/2}$ is the excited state manifold, otherwise it is $3^2P_{3/2}$.

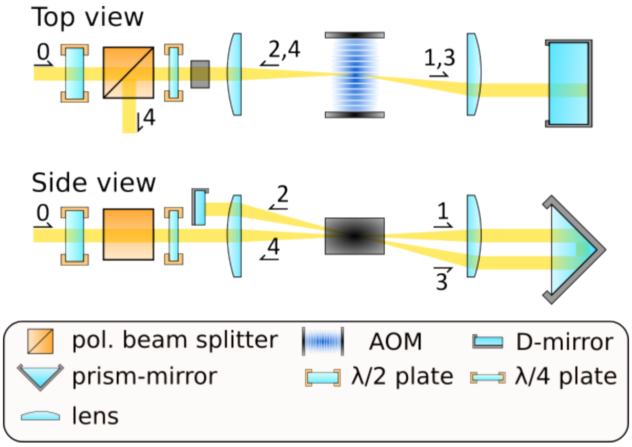

Figure 3.4: Overview of the AOM quadruple pass used to generate sodium repumper light. A prism mirror is employed to introduce a vertical offset to the first order of the first pass, making two additional passes possible by retro-reflection of the second pass using a "D"-shaped mirror. Figure adapted from [24].

beam, since it requires a lot of power (in total around $400\mathrm{mW}$ after the fiber), while every other AOM path received light from the leader laser. With the new system, we exchanged one of the *TOPTICA Photonics TA-SHG-Pros* for the aforementioned fiber laser. With its high power output of $4\mathrm{W}$ it is possible to generate the slower beam by virtue of an additional AOM double pass with a free space EOM in front of the fiber to add the repumper side bands. Now, the laser previously labeled as "leader"-laser can be used to generate $1.3\mathrm{W}$ of D_1 light, which is plenty of power for the grey molasses cooling (we only need about $80\mathrm{mW}$ in total in front of the fiber). A schematic of the whole new sodium laser setup is shown in Figure 3.5, the section shifting the D_1-light to the desired frequencies[3] can be seen in Figure 3.6. This light is overlapped with the beams used for the 3D MOT and coupled into the same fiber. For details on planning and design choices of the restructuring of our laser system and implementation of the grey molasses refer to Malaika Göritz' master thesis [16].

3.1.4 *Light Amplification for Potassium*

With the lasers being stabilized to the desired frequencies, we need to amplify them, since the power output of this model of laser is limited to roughly $20\mathrm{mW}$ to $30\mathrm{mW}$ per unit. For reaching the powers needed to operate the MOT and grey molasses stage, we utilize Tapered Amplifiers (TAs), which are semiconductor optical amplifiers with a distinct tapered geometry, hence their name. These chips consist of two sections (see Figure 3.7): A $3\mu\mathrm{m}$ wide wave guide section for transferring a single mode to the amplifying part of the chip. Here, the tapered shape allows the amplified light to diverge through the gain medium in the horizontal direction, enabling high amplification without reaching problematic energy densities which could damage the chip.

Operating TAs involves focusing the seed laser into the waveguide and collimating the highly divergent output. To achieve this we use a compact fiber-coupled module designed by Florian Nicolai (see [29], an overview is shown in Figure 3.8). The central piece consists of a copper block which houses the tapered amplifier chip[4]. It uses a pair of aspheric lenses with $f = 4.51\mathrm{mm}$, the focal points of which should align with the center of the chip. A cylindrical lens with $f = 40\mathrm{mm}$ is used to collimate the beam in the horizontal direction afterwards. This lens is crucial for coupling into the output fiber, which is why it is mounted in a precision rotary mount attached to a transition mount for changing its position along the beam path (this change improved the

---

[3] We usually refer to these two frequencies as "D_1-cooler" and "D_1-repumper", even though their roles are quite different than the beams with the same name in a MOT. In the grey molasses, both frequencies are needed in conjunction for the relevant two-photon-transition, where the beams in the MOT excite separate single photon transitions.

[4] We use the model "Eagleyard Photonics EYP-TPA-0765-02000".

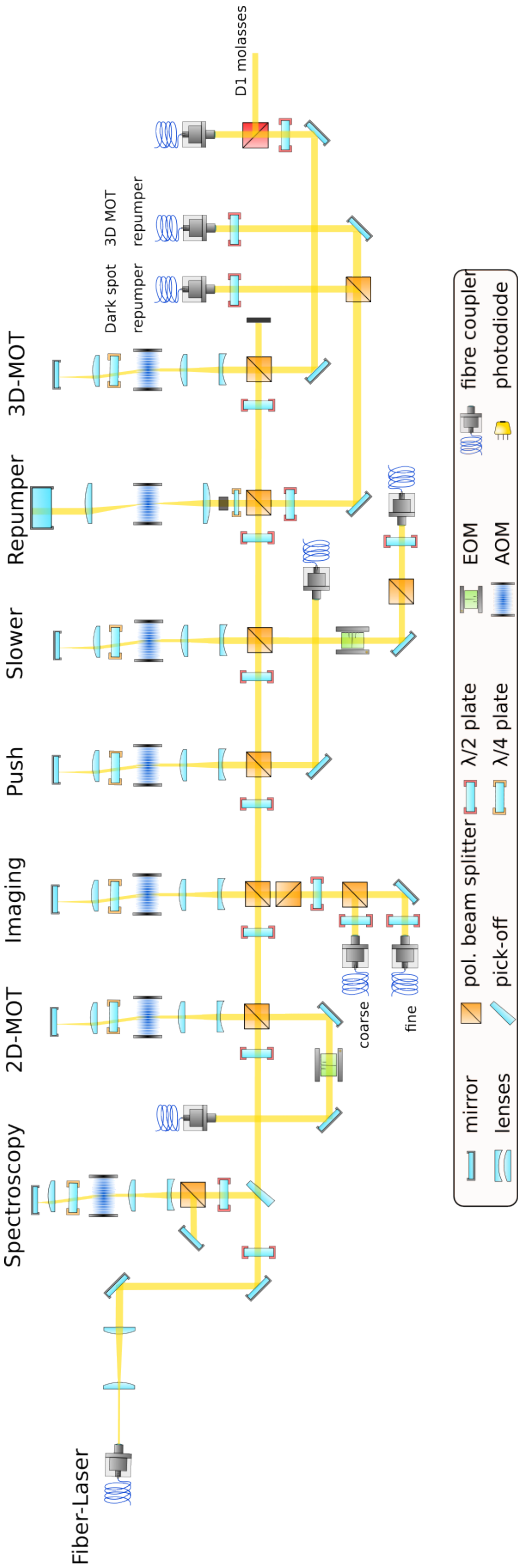
Fiber-Laser
Spectroscopy
2D-MOT
Imaging
Push
Slower
Repumper
3D-MOT
Dark spot repumper
3D MOT repumper
D1 molasses
coarse
fine
mirror
lenses
pol. beam splitter
pick-off
λ/2 plate
λ/4 plate
EOM
AOM
fibre coupler
photodiode

Figure 3.5: Overview of the sodium laser table containing all AOM-paths and EOMs (rotated for space reasons). The AOM- and EOM-frequencies are noted in Table 3.1. Figure adapted from [16].

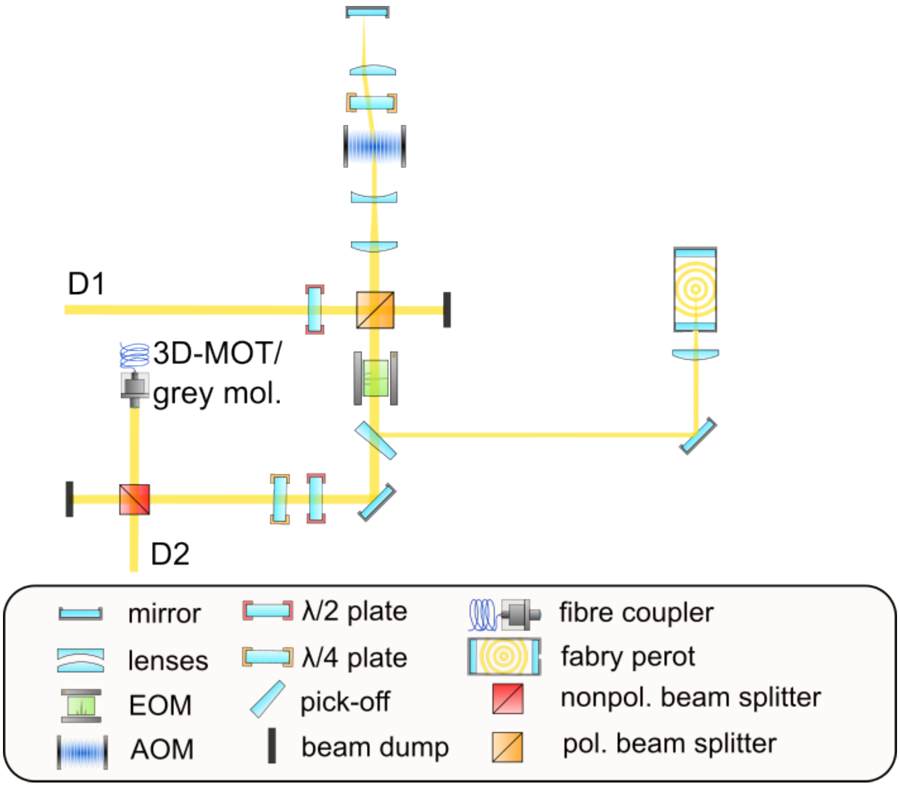
D1
3D-MOT/
grey mol.
D2
mirror
lenses
EOM
AOM
λ/2 plate
λ/4 plate
pick-off
beam dump
fibre coupler
fabry perot
nonpol. beam splitter
pol. beam splitter

Figure 3.6: Optical layout of the sodium-D_1-setup. The AOM is used to shift Δ, the EOM generates the repumper sideband. A Fabry-Pérot-Interferometer is employed to monitor the intensity of the repumper. Figure adapted from [16].

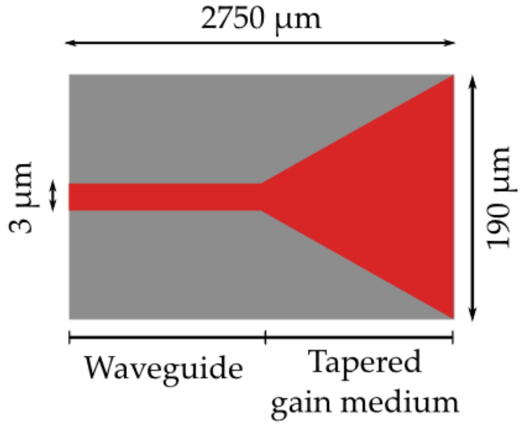

Figure 3.7: Sketch of the geometry of a TA diode (from [23]).

final coupling efficiency by 15%, for details see [17]). To mitigate any back reflections, a Faraday isolator is employed directly after, which has a maximal transmission rate of roughly 80% [5]. This component is crucial, since any back reflection making it into the tapered gain medium of the the chip from the wrong direction will be amplified, but in this case the tapered shape will focus light into the waveguide, which can result in destroying the chip. We use single mode fibers to transport the seed beam to the module and also to transport the output beam to its desired location. A lamda half plate is used in front of the output beam fiber coupler to ensure polarization maintaining coupling. Lastly, two pairs of folding mirrors are employed for coupling and to make the whole setup more space efficient. All optical components of this module are mounted on a 10kg aluminum plate, which not only acts as a heat sink for the thermal energy produced by the high currents running through the TA (around 3A), but also enables high flexibility of the modules position on the laser table.

Our potassium laser system relies on three such TA modules for light amplification: the first has been dubbed the "Main TA" and its seed comes directly from the laser locked on the D2 line of potassium. Its output is used to generate the light for the 2D and 3D MOT and also for the absorption imaging. The 2D MOT requires a lot of power, which is why only a small fraction of the Main TAs output is shifted to the 2D MOT cooler and repumper frequencies (see Table 3.3 for more information). These beams will then be overlapped to generate the seed beam of the second TA, the "2D MOT TA", the output of which will go directly to the experiment table.

Because of various circumstances involving different experiments in this group, the optical amplifier chip of the 2D MOT TA had to be replaced at one point. After realigning the seed beam to the new chip

---

[5] This efficiency can be optimized by placing the Faraday isolater in the beampath and rotating it around the beam axis.

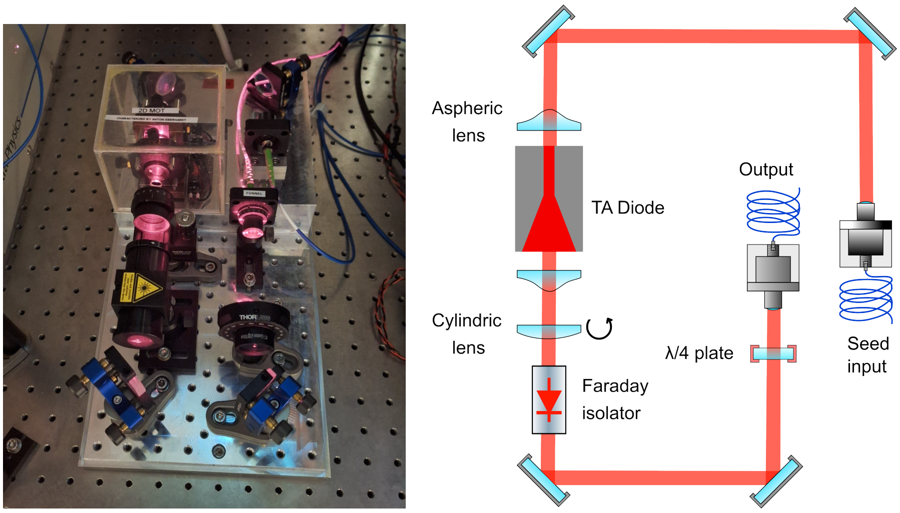

(a) Image of the 2D MOT TA (b) Schematic overview of the TA module

Figure 3.8: Illustrations of a TA module used in our experiment

	Seed power $[\mathrm{mW}]$	Output power $[\mathrm{mW}]$	Power after fiber $[\mathrm{mW}]$
Main TA	12.6	1460	620
2D MOT TA	14.0	1360	490
D1 TA	17.0	1050	500

Table 3.2: Performance of the Potassium TAs. The output power was measured after the Faraday isolator.

and recoupling the output beam I characterized the chips behavior with various measurements which can be found in Section 3.1.5.

For the third TA the laser locked to the D1 line is employed as seed beam, therefore it was named "D1 TA". Its output will be further prepared for the gray molasses stage (see Section 4.4.4). An overview of seed power, output power and coupling efficiency of each TA is given in Table 3.2. A full overview of the potassium laser table is given in Figure 3.9.

3.1.5 *2D MOT TA characterization*

In this section I present the results from quantitative measurements regarding the performance of the TA chip used in our "2D MOT TA" module. The amount of gain produced by the chip can be adjusted via the external current running through it, as can be seen in Figure 3.10. It is important to note that the ratio of decoherent light generated via Amplified Spontaneous Emission (ASE) to the amount of coherent amplified light decreases with higher currents, which becomes clear when looking at the fiber coupling efficiency, since the amount of ASE that can be coupled into a single mode fiber is very limited: At $3\mathrm{A}$

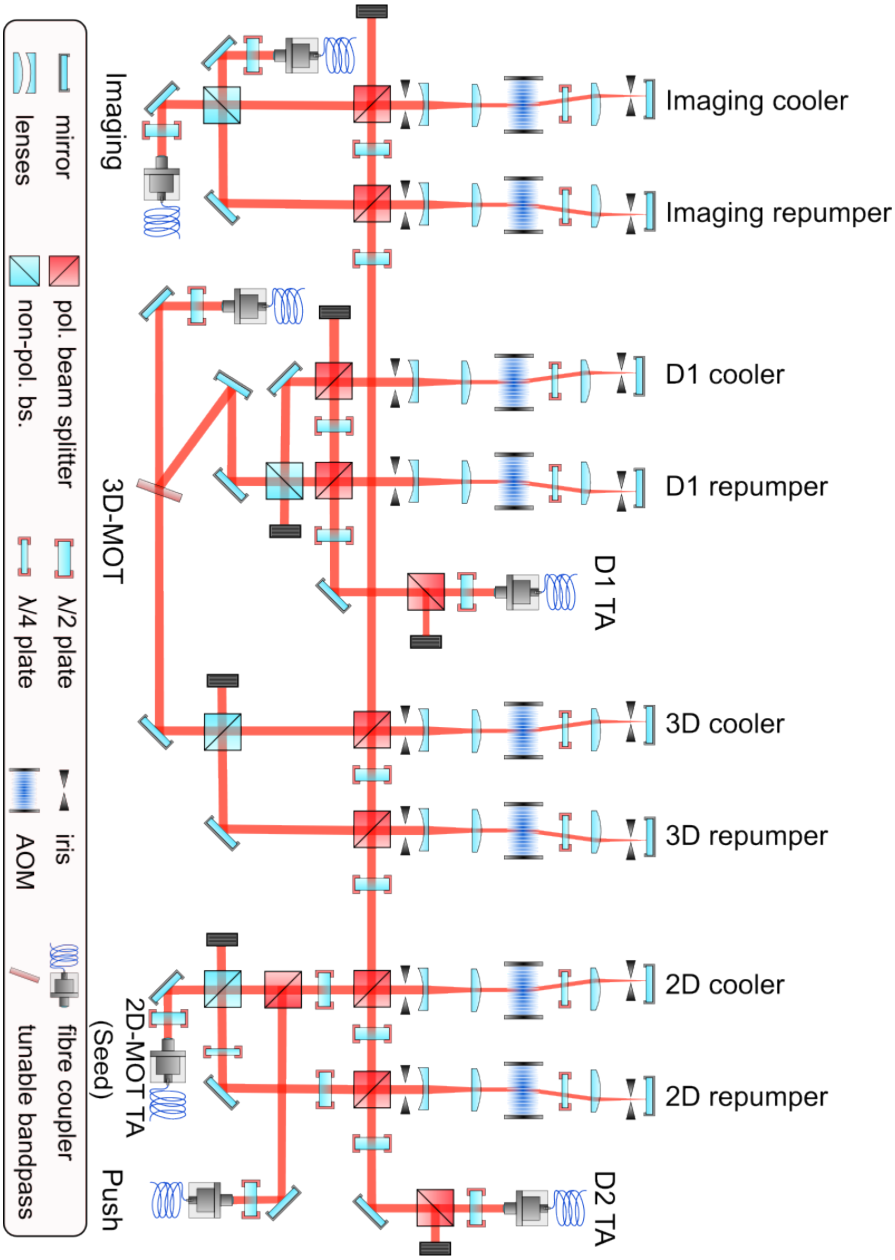
Imaging cooler
Imaging repumper
D1 cooler
D1 repumper
D1 TA
3D cooler
3D repumper
2D cooler
2D repumper
D2 TA
Imaging
3D-MOT
2D-MOT TA
(Seed)
Push
mirror
lenses
pol. beam splitter
non-pol. bs.
λ/2 plate
λ/4 plate
iris
AOM
fibre coupler
tunable bandpass

Figure 3.9: Setup on laser table to generate light necessary for cooling and imaging potassium (rotated for space reasons, figure adapted from [24]).

	Transition $\vert F\rangle \to \vert F'\rangle$	Detuning $[\mathrm{MHz}]$	AOM/EOM frequency $[\mathrm{MHz}]$
2D MOT cooler	$\vert 2\rangle \to \vert 3\rangle$	-31	-121
2D MOT repumper	$\vert 1\rangle \to \vert 2\rangle$	-13	+108
3D MOT cooler	$\vert 2\rangle \to \vert 3\rangle$	-10	-110
3D MOT repumper	$\vert 1\rangle \to \vert 2\rangle$	-8	+111
Imaging cooler	$\vert 2\rangle \to \vert 3\rangle$	-1	-112
Imaging repumper	$\vert 1\rangle \to \vert 2\rangle$	-6	+112
D_1 cooler	$\vert 2\rangle \to \vert 2\rangle$	+19	-113
D_1 repumper	$\vert 1\rangle \to \vert 2\rangle$	+19	-118

Table 3.3: Detunings and AOM-frequencies for the $^{39}\mathrm{K}$ laser setup. Every entry corresponds to a AOM double pass (see Figure 3.9). Entries with D_1 in their name have the $4^2P_{1/2}$ as their excited state manifold, otherwise it is $4^2P_{3/2}$.

we achieved a coupling efficiency of around 35%, resulting in around $490\mathrm{mW}$ of power on the experiment table, however, at $1.5\mathrm{A}$ we only achieved around 10% coupling efficiency. At very high currents (above $2.8\mathrm{A}$), the output mode of the TA deteriorates, leading to a decrease of coupling efficiency, which is why $3\mathrm{A}$ is chosen as the operating current.

In contrast to the other two TA modules used in our laser setup, the 2D MOT TA's output should contain two frequencies instead of one, since it is used to amplify both the cooler and the repumper light for the 2D MOT. For potassium, the ratio of cooler to repumper light should be roughly one to create an approximately closed optical cycle [18], yet using this ratio for the seed beam does not provide desired output, which I first naively expected. It turns out that frequency response of TA diodes is not trivial and that both frequencies compete for gain, leading to regions of instability, where thermal effects and fluctuations from other sources can strongly disturb the resulting spectrum.

Using a Fabry-Pérot-Interferometer located after the output fiber on the experiment table, I investigated different settings for the seed beam power ratios in order to find a stable configuration with the correct ratio between the frequencies, which are summarized in Figure 3.12. Each point in this graph corresponds to roughly 20 Fabry-Pérot spectra acquired using an oscilloscope (an example can be seen in Figure 3.11), which were taken in a span of around 5 minutes for each seed beam configuration. The height of each peak was extracted using Python[6] and the relative peak height of the cooler and repumper frequencies is used as a measure for their power ratio. During this measurement, the total power of the seed beam was kept constant at $12\mathrm{mW}$, while the power distribution between the two frequencies was varied by turning the $\lambda/2$-waveplates in front of the AOM paths (see Figure 3.9).

---

[6] I used the function `scipy.signal.find_peaks`

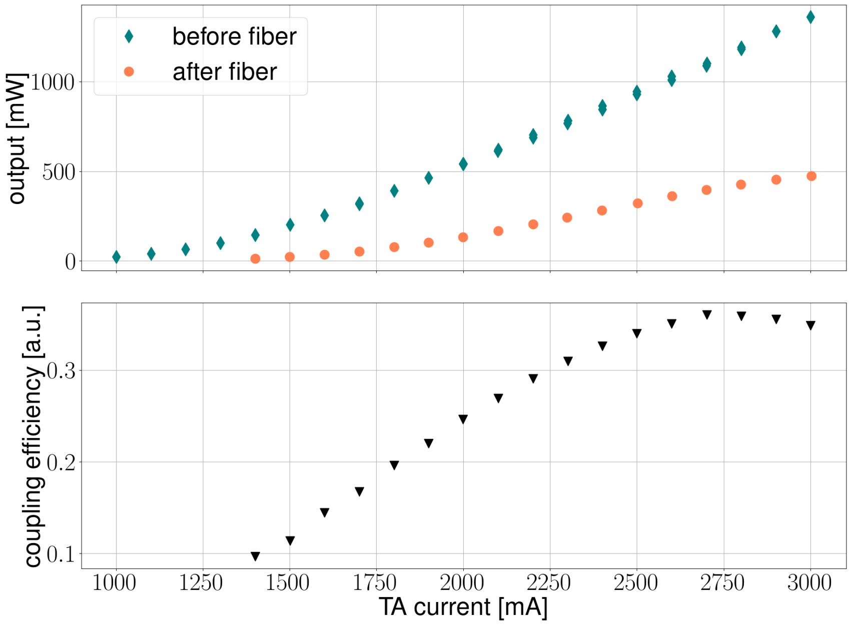

Figure 3.10: (Upper panel) Measurement result for the output power of the 2D MOT TA over the applied current. The seed power for this measurement was $11.6\,\mathrm{mW}$, which corresponds to the seed power during regular operation of the experiment. (Lower panel) Coupling efficiency of light amplified by the TA.

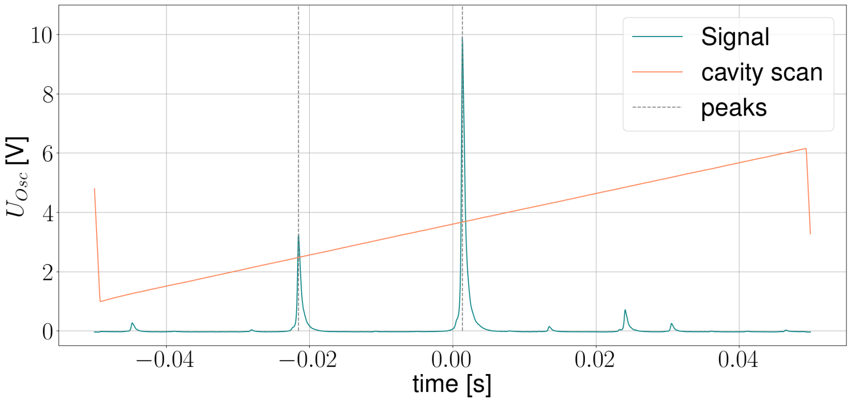

Figure 3.11: Example of the output beam spectrum of the 2D MOT TA acquired using a Fabry-Pérot-Interferometer and an oscilloscope. The middle peak corresponds to the cooling light, the peak to the right corresponds to the repumper.

As mentioned before, the output spectrum we are aiming for should contain equal parts cooler and repumper light while also being stable in time. With this in mind, the first measurement in Figure 3.12 (blue diamonds), where the seed power ratio was measured before the seed fiber, shows that only a few points in the probed range actually fulfill the first requirement, surprisingly two of them being at $P_{Cooler}/P_{Repumper} \ll 1$. Additionally, these seed beam configurations also seem to show the lowest relative standard deviation across the 20 snapshots taken using the oscilloscope, which means they seem to be the most stable at this timescale. The only other point which would be usable for everyday operation is around $P_{Cooler}/P_{Repumper} = 0.5$, although the variance is a bit larger.

Another interesting behavior I observed in the first measurement is that there seem to be multiple points at which the dominating frequency switches, instead of only one point. For the majority of the measurement, the cooler light was clearly being amplified more strongly. However, there were a few regions where the largest peak in the spectrum corresponds to the repumper light (so $U_{Cooler}/U_{Repumper} < 1$), but next to each of these regions, the cooler light was again dominating, where I would have expected one setting with equal parts cooler and repumper, with mostly repumper for smaller ratios and mostly cooler otherwise.

These discrepancies lead to performing a second measurement with some improvements: First I checked the polarization maintaining coupling of the seed fiber using a polarization analyzer[7], which had been optimized before. Because of the 2 frequencies, this also requires more work than usual, because each frequency needs to have polarization maintaining coupling separately and both should have perfect horizontal polarization after the seed fiber, since this is the mode that the TA chip preferably amplifies. This necessitates, that both frequencies have exactly the same polarization in front of the fiber, which is why an additional $\lambda/4$-plate was added before the non-polarizing beamsplitter in the repumper path (here, cooler and repumper are overlapped, see Figure 3.9) during the previous optimization. At the time of the second measurement, the polarization was quite close to optimal and only needed slight adjustments.

The other difference to the first measurement is that I now measured the seed powers directly after the seed fiber, so exactly how it enters the TA and I blocked the cooler beam at a improved position when measuring the repumper power[8]. This also reduced stray light hitting the power meter, which could have influenced the measured ratios in the first measurement.

---

[7] Model *Schäfter+Kirchhoff Polarization Analyzer SK010PA*

[8] In the first measurement, I blocked the beam in front of the non-polarizing beamsplitter. If the polarization after the cooler AOM double pass was not ideal, some of the cooler light could have been reflected back to the repumper path. This could've caused more cooler light to make it into the fiber than the measured ratio would suggest. For the second measurement I blocked the beam directly after the repumper AOM path.

In the second measurement (orange circles in Figure 3.12) I focused on the regions where the first measurement gave confusing results, as well as the mirrored case, where $P_{cooler} \gg P_{repumper}$ to see if the unintuitive frequency response is reversible. In these results, the output ratio seems to tend towards zero for very small ratios of $P_{cooler}/P_{repumper}$, contrary to the behavior during the first measurement. My guess is that there is a sizable error on the calculated ratios (i.e. each points position on the x-axis) in the first measurement. These issues seem to have significantly improved with the adjustments that were made for the second measurement. Still, the optimal setting seems to be at a ratio of roughly 1:10. Also, when reversing the roles (so a lot of cooler and a small amount of repumper) we do not see similar behavior, as the cooler light is amplified a lot more for all points above a ratio of 1:10 like in the first measurement.[9]

In summary, we found a good setting for everyday operation with this experiment, however, it is still not clear how the highly unbalanced frequencies in the seed beam lead to a 1:1 output after the TA. To investigate this further, one could do an experiment where the seed beam configuration does not change, but the carrier frequency or the individual AOM-frequencies are varied. With this, one could potentially visualize if the gain is actually frequency dependent when operating the chip with multiple input frequencies. The overall amplification did not seem to have a significant frequency dependence in this range, since the overall output power never changed drastically during all of the previous measurements, even though the input frequencies were varied.

3.2 VACUUM SYSTEM AND ATOM SOURCES

3.2.1 *Two dimensional Magneto-Optical-Traps (2D MOT)*

Crucially, the lifetime of atoms in the 3D MOT (as well as in all subsequent trapping stages) is limited by collisions with untrapped particles of the surrounding gas, which makes it desirable to operate the main part of our experiment in Ultra High Vacuum (UHV) [25]. This, in return, necessitates a directed beam of preferably cold atoms that comes from outside the UHV. In our experiment these atomic beams are generated by a two dimensional MOT for each species, the designs of which were inspired by the work of G. Lamporesi et al. [25] and T.G. Tiecke et al. [44]. An in depth discussion of 2D MOT and vacuum chamber design choices specific to our experiment can be found in [20]. A sketch of

---

[9] During the second measurement, I also measured at $P_{cooler}/P_{repumper} \approx 35$, however the peak representing the repumper became so small in this region that it was not measurable with the Fabry-Pérot-Interferometer anymore.

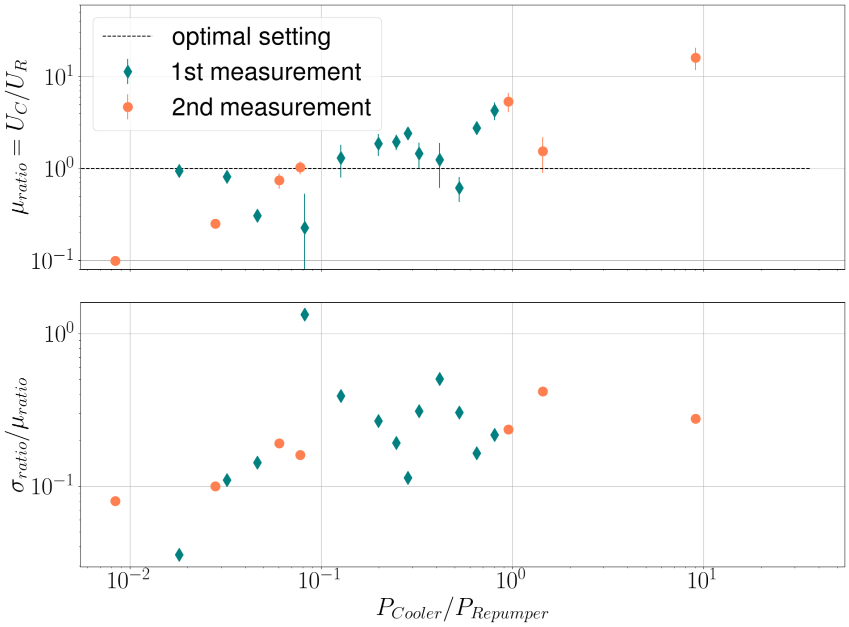

Figure 3.12: (Upper panel) Measurements of the 2D MOT TAs output power dependence on the power ratio of cooler and repumper light in the seed beam. Each data point represents the mean of 20 separate Fabry-Pérot-Spectra for the same setting. The red bars represent the standard deviation. (Lower panel) Relative fluctuations of the ratios seen in the upper panel to estimate the stability of each setting.

our system can be seen in Figure 3.13, where the vacuum chambers housing the 2D MOTs are located to the left. They are seprated from the UHV-region (the "science chamber") on the right by differential pumping stages and gate valves.

As the name suggests, the method utilizes exactly the same principles as the 3D MOT described above, but without cooling beams along one dimension[10], so atoms won't be slowed down in this direction. While other groups usually use two cooling beams which are retroreflected (e.g. [44]), our setup employs 4 separate beams, allowing for more control on beam balancing and alignment.

The 2D MOTs are loaded by ovens located below the beam crossing, which originally contained $1\,\mathrm{g}$ of sodium and potassium respectively. For the latter, the oven is heated to $60\,^{\circ}\mathrm{C}$, while the sodium oven is operated at around $160\,^{\circ}\mathrm{C}$. It is worth noting that the sodium 2D MOT also features an additional beam of cooling light (usually referred to as "Zeeman slower beam" [20, 25], since this beam together with the magnetic gradient field acts as like small Zeeman slower), which enters from the top and shines directly into the oven. The presence of this beam increases the loading rate into the 3D MOT[11] by an order of magnitude [20, 25].

The quadrupole magentic field required for operation is generated by four stacks of permanent neodymium bar magnets which are mounted on the outside of the vacuum chamber [19]. Lastly, a so called "push beam" is employed for both 2D MOTs, which is also red-detuned and points toward the location of the 3D MOT. It "pushes" atoms moving away from the science chamber back towards it while leaving atoms already moving in the correct direction largely unperturbed, therefore drastically improving the loading rate.

3.2.2 *Optimizing the 2D MOTs*

In this section I will give a short account of our optimization procedure for the atom sources. For us, the most practical way is to use the signal in the 3D MOT, which can be measured either by utilizing the absorption imaging system (Section 3.3) or by a photodiode hooked up to an oscilloscope and looking directly into the science chamber. This photodiode measures the florescence of the 3D MOT, giving a relative measure of how many atoms are currently present in the trap[12]. As mentioned before, the loading rate can be a good indicator of the 2D MOT's performance and using the photodiode, a signal generator, and

---

[10] In our setup, the 2D MOTs are arranged such that the axis along which the atoms are not slowed down connects the centers of the 2D and the 3D MOTs.

[11] This loading rate is the main criterion by which we usually judge the performance of our 2D MOTs, since it is closely related to overall atom flux originating from them.

[12] Note that this approach does not work well when using the dark SPOT, since here the majority of trapped atoms does not scatter any light. When optimizing the 2D MOT, we use regular repumper beams instead of the ones with donut-shape

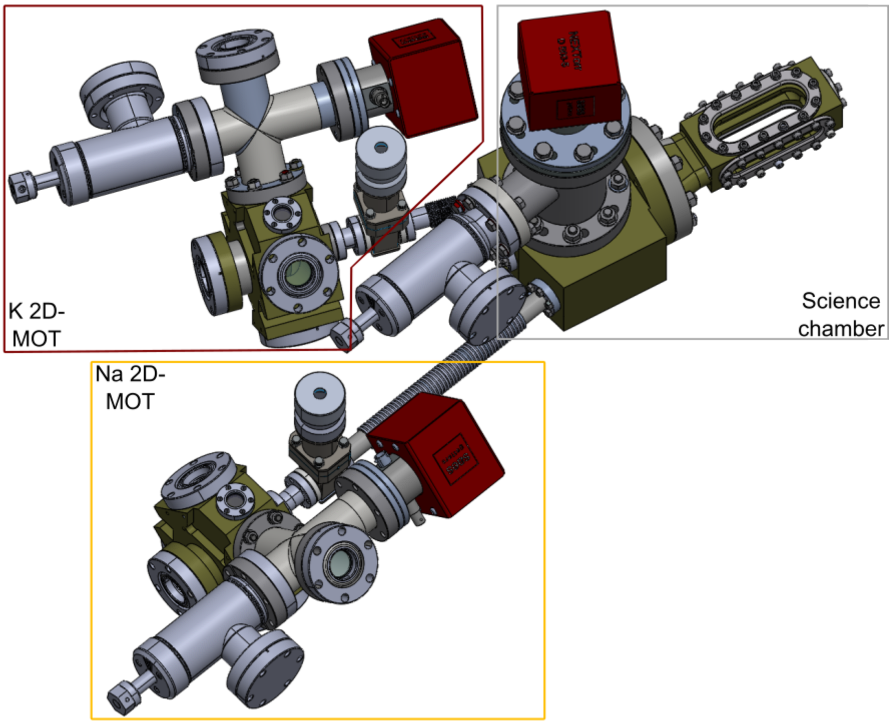
K 2D-
MOT
Science
chamber
Na 2D-
MOT

Figure 3.13: Illustration of the vacuum system, viewed from the top. The housings of the ovens are located below the respective 2D MOT chambers (not visible in this picture). The red cubes are ion-getter pumps (Model: *SAES NEXTorr Z100/D500*).

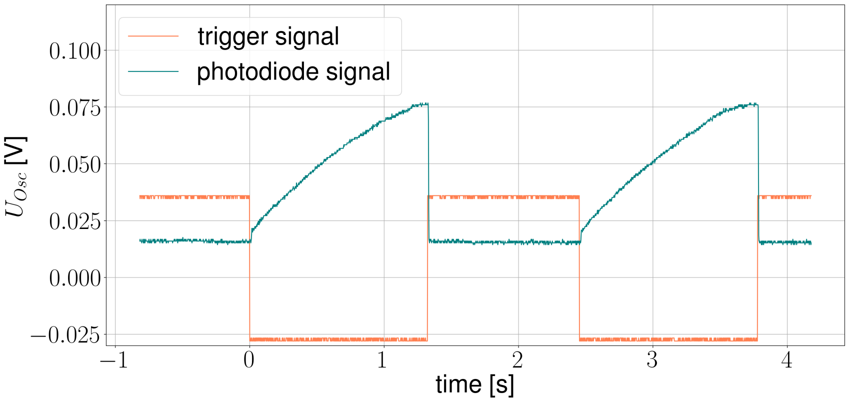

Figure 3.14: Example for the signal we use to optimize the 2D MOTs. The trigger signal is used to periodically open a mechanical shutter, which blocks the 3D MOT beams when closed. A photodiode is used to measure the florescence of the 3D MOT (the potassium 3D MOT in this case). The signal can be viewed with an oscilloscope (which was also utilized to capture this data). The trigger signal was scaled down by a factor of 150 for visibility reasons.

a mechanical shutter, this can be very easily measured: The shutter is placed in the beam path of the 3D MOT cooling light while the signal generator is used to trigger it and the oscilloscope by applying a suitable square wave signal. We want to avoid saturation of the loading curve, where losses due to high trap densities become dominant, which is why the frequency on the signal generator is increased until only the linear part of the loading curve is visible. This way, we avoid systematic errors that could arise from an imperfect state of the 3D MOT which are largely unrelated to the atom source. The frequencies we use are usually between $0.5\mathrm{Hz}$ and $2\mathrm{Hz}$, which is fast enough to essentially optimize most parameters in real time and fully analog, instead of having to run sequences and waiting for the software to analyze the results. An example for a loading curve as seen on the oscilloscope is given in Figure 3.14.

3.2.3 *Sodium Oven Issues*

Naturally, it is crucial that there is enough of the desired element present in the oven at all times to ensure efficient loading of the 2D MOTs. If this is not the case, a refill is required, which necessitates breaking the vacuum, filling up the oven and subsequently baking out the 2D MOT's vacuum chamber to remove any contamination (like for example water) that can enter the system during such a process. This in itself is quite time consuming, but refilling the oven also requires the removal of many optics surrounding the vacuum chamber, which is why we are reluctant to do this.

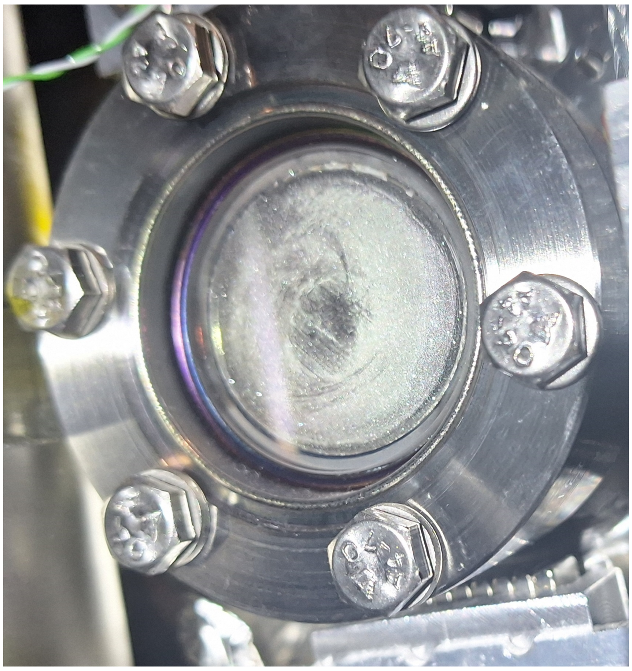

Figure 3.15: Picture of the sodium depositions on the push beam viewport, which is currently not heated. The lower viewports looked very similar before heating them. The "clear" spot is where the push beam usually enters the chamber, it seems that the sodium depositions are suppressed here.

During the last year, there was a prolonged duration in which we noticed a steady decline of sodium atom numbers across all stages of our cooling sequence. We noticed that the viewports of the sodium 2D MOT were obscured by what looked like a metallic film, assumingly sodium depositions that had built up over the last view months of operation (Figure 3.15 shows an example of such depositions). This issue was something that was anticipated, since it already happened at this experiment before. Previously, the upper viewports have been more prone to these kinds of depositions, since they are directly facing the oven, which is why it was decided to permanently heat them to around $100°\mathrm{C}$. However, we now noticed that the lower viewports were affected more strongly, leading to only around 50% of the laser light being transmitted through the chamber. Since the upper viewports were not affected as heavily (probably due to the heating), we decided to switch the position of the heating clamps to heat the lower viewports instead of the upper ones[13].

This is when we noticed that the florescence of the push beam going through the 2D MOT increased dramatically (see Figure 3.16). Also, the loading rate (measured using the method described in the previous section) also showed a significant increase while the transmission through the chamber had not really improved yet. Some further investigation showed that there were sizable sodium deposits in the shape of large droplets all around the inside of the vacuum chamber, two of which are also visible in Figure 3.16. From this observation, we hypothesized that the sodium that was originally located in the oven is mostly used up, but this can be compensated by heating different parts of the chamber. This hypothesis was also supported by two additional observations:

---

[13] Initially, we decided against heating both the upper and the lower viewports simultaneously, since we were concerned that this would increase the temperature of the bar magnets, potentially damaging them.

- We immediately noticed that the ion pump located in the sodium 2D MOT chamber registered a significant increase in ion pump current (which usually is indicative for a pressure increase) after we started to heat the lower viewports. We are constantly monitoring the pump currents for all three of our ion pumps, since a strong increase here could be an early warning for potential vacuum problems[14] and Figure 3.17 shows the monitoring data from the time when we started heating the lower viewports. Ion pump currents shouldn't be interpreted as a direct measure for the pressure inside the chambers, but the two variables are usually strongly correlated, so we regarded the strong increase as direct cause of the heating of the lower viewports.
- During the last few months, we sometimes adjusted the sodium oven temperature to see its effect on the overall atom number in the 3D MOT. At the point of writing this, lowering the oven temperature from $170°\mathrm{C}$ to $25°\mathrm{C}$ (room temperature) doesn't seem to influence this number very much, which could indicate that the sodium we are currently loading doesn't come from the oven, but from some other part of the chamber. When letting the oven sit for a few days at room temperature and then turning it on again, we also only see a slight increase in atom number and loading rate, instead of a large jump that would be expected if sodium is still present in the oven.

However, we also observed that the slower beam still had a quite significant effect on the loading rate. If the oven was empty and sodium is evaporated mostly from depositions around the whole chamber, we would have expected that the effect of the slower beam would also diminish, since in theory it preferably slows atoms coming directly from the oven, however, we did not observe such a decrease. To test this further, we blocked the slower beam and tried to optimize the rest of the 2D MOT without it, since the slower alters the scattering force and the optimal parameters for the rest of the 2D MOT should be quite different with the slower compared to without it. Still, after we finished optimizing, the loading rate was only a small fraction of what could be achieved with the slower beam turned on. We think that the large effect the slower still seems to have can be explained by the possibility that there are large sodium deposits still near, but not in the oven, which are passively heated by the heating clamps on the lower viewports. Additionally, the atoms coming directly from the lower viewports would also posses a significant velocity component in the direction of the slower beam if they arrive in the trap center largely unperturbed.

---

[14] Although so called "leakage current" could also cause similar strong increases, as we have learned very recently. This issue is described in more detail in [20].

Since it is not very practical to switch the position of the heating clamps around whenever the atom number decreases, we had the idea to heat the whole sodium 2D MOT chamber in the long term. This way, the positions of the sodium depositions don't matter and it could also help in keeping all the viewports clean without having to heat them individually. An issue with this could be that the neodymium magnets we are currently using for the gradient field have an operating temperature of $80°\mathrm{C}$ and below, so before heating the whole chamber to around $100°\mathrm{C}$ we will have to exchange all our magnets with one made out of samarium-cobalt (SmCo32), which have a working temperature of up to $350°\mathrm{C}$ (more details can be found in [20]). It will also be interesting to see if the effect of the slower will be different when heating the whole chamber. Until now, we are still operating the experiment with the original magnets while heating all viewports except the push beam viewport. When starting to heat all viewports, we monitored the temperature of the magnets to ensure they do not exceed their operating temperature.

3.3 ABSORPTION IMAGING SYSTEMS

While measuring the florescence of the 3D MOT using a photodiode can give a decent relative estimate on the amount of trapped atoms, for optimizing the dark SPOT and all subsequent cooling stages a different detection method needs to be employed. We use the widely known absorption imaging [21], where a resonant beam of light is guided through the atomic cloud and onto a CMOS camera. Using Beer-Lambert's law, we can relate the amount of absorbed light to the column density $n(x, z)$ of the atoms, where x and z are the coordinates in the imaging plane:

$$I(x, z) = I_0(x, z) e^{-n(x,z)\sigma_{eg}} \tag{10}$$

$I_0(x, z)$ and $I(x, z)$ are the intensities of the beam before and after traversing the atomic cloud and $\sigma_{eg} = \frac{3\lambda^2}{2\pi}$ represents the absorption cross section, which depends on the wavelength of the laser λ [24]. In practice, we are interested in the optical density of the cloud, which is given by

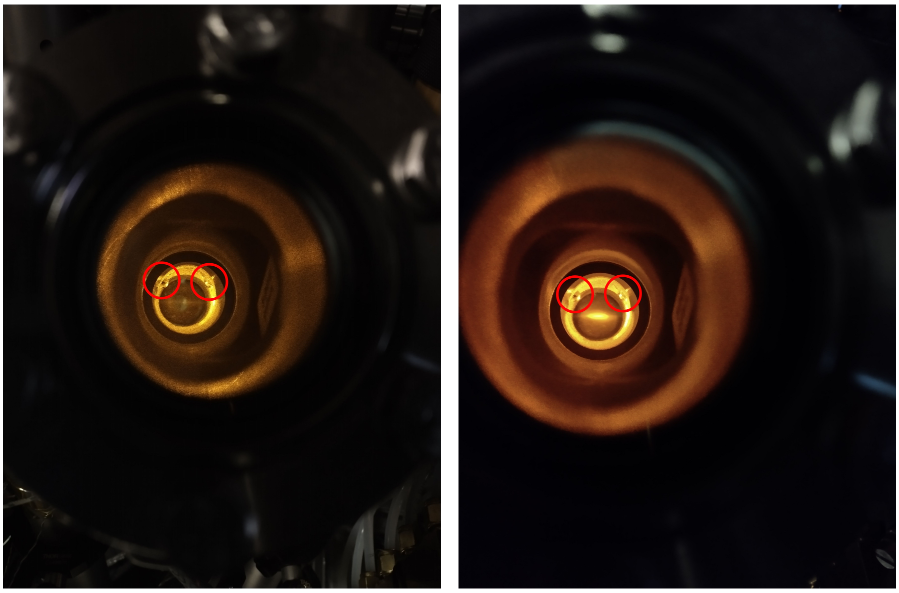

(a) Lower viewports heated to 90°C (b) Lower viewports heated to 99°C

Figure 3.16: Pictures taken looking through the slower viewport for different temperatures of the lower viewports. One can clearly see the florescence increasing with the higher temperatures. The visible sodium deposits are marked with red circles.

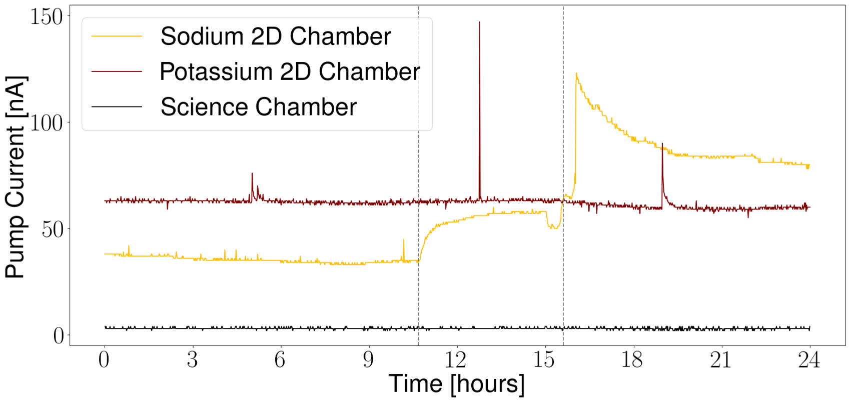

Figure 3.17: Ion pump currents from all three pumps during the time when we first started heating the lower viewports. The first dotted grey line marks the start of the heating process, which is direcly followed by a rise of ion pump current in the sodium 2D MOT chamber. The second grey dotted line marks the point where the temperature of the viewports exceeded the melting point of sodium, which is 97.8°C. This also caused a spike in measured the ion pump current.

$$OD(x,z) = n(x,z)\sigma_{eg} \tag{11}$$

This quantity can be measured by taking three images: The first image (represented as the intensity distribution $I_{atoms}(x,z)$) is taken directly after the TOF, so a portion of the imaging beam is absorbed by the atoms. The second image ($I_{reference}(x,z)$) is taken after a delay of $200\mathrm{ms}$ to ensure that no atoms are present to absorb light[15]. Thus, this image only contains the unperturbed imaging beam profile. Lastly, a third image is captured ($I_{dark}(x,z)$), this time without turning on the imaging beam to measure the noise floor of the camera sensor. Finally, we can calculate the optical density distribution as follows:

$$OD(x,z) = -\ln\left[\frac{I_{atoms}(x,z) - I_{dark}(x,z)}{I_{reference}(x,z) - I_{dark}(x,z)}\right] \tag{12}$$

In SoPa, we have two separate absorption imaging systems, an overview of how they are set up is shown schematically in Figure 3.18. The low resolution imaging ("coarse imaging") features a camera[16] with a 484 by 644 pixel sensor and a pixel size of $7.4\mathrm{\mu m}$. The imaging path is set up to image the MOT, molasses and magnetic trap and has a magnification of $M_{coarse} = 0.445$. For imaging the crossed optical dipole trap (cODT) ("fine imaging"), we use a CMOS camera[17] with much higher resolution of 2560 by 2160 pixels and a pixel size of $6.5\mathrm{\mu m}$. The magnification of this imaging setup was measured to be $M_{fine} = 20.38(3)$ (see Section 4.3.2). To image both species along the same beam paths, we employ dichroic mirrors for overlapping and splitting the beams. For more information on both imaging setups, see [24]. It is worth noting that the glass of one of the science chamber's viewports has a scratch, which is located directly inside the the beam path of the coarse imaging. This causes artifacts in the measurements taken with this imaging system, which will be visible in some of the pictures presented in the upcoming chapters.

---

[15] The resonant imaging light pulse of the first picture already removes most of the atomic cloud from the camera frame, since the atoms are heated by the resonant excitations and diffuse outwards. With the additional delay of $200\mathrm{ms}$ the possibility of remnants of the sample being captured on the reference picture is basically zero.

[16] *Allied Vision Mako G-030 B*

[17] *Andor Zyla 5.5*

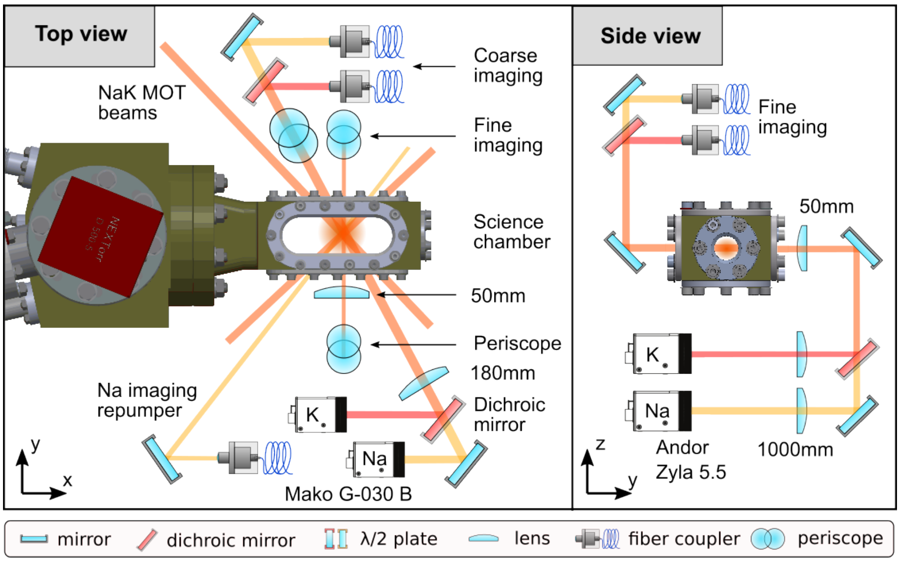
Top view
NaK MOT beams
Coarse imaging
Fine imaging
Science chamber
50mm
Periscope
180mm
Dichroic mirror
Na imaging repumper
K
Na
Mako G-030 B
y
x
Side view
Fine imaging
50mm
K
Na
Andor Zyla 5.5
1000mm
z
y
mirror
dichroic mirror
λ/2 plate
lens
fiber coupler
periscope

Figure 3.18: Overview of the two imaging systems used for measurements of the density distributions of trapped atoms. The coarse imaging uses a single lens and lokks at the science chamber with an angle, such that the imaging beam is almost parallel one of the horizontal MOT-beam-pair. The fine imaging is aligned to be symmetric to the MOT-beams and uses two lenses to facilitate higher magnification. The imaging beams for sodium and potassium are overlapped directly after the fiber coupler using dichroic mirrors. Right before the camera, another dichroic mirror splits the beams apart and guides them toward their respective cameras. The figure was adapted from [24].

4

OPTIMIZATION OF THE COOLING SEQUENCE

I will begin this chapter by outlining the sequence of cooling steps we used to successfully produce a sodium condensate for the first time. As before, I will explain the optimization process and detail the challenges each step involved. Afterwards, I will describe some significant changes in our laser cooling approach, which we think will help us to achieve dual species degeneracy.

4.1 PREVIOUS SEQUENCE

In our experiment, sodium is should as a sympathetic coolant for potassium [24]. The principle at work here is that potassium sits deeper in the cODT due to gravitational sack and a different polarizability of the two species. Thus, evaporative cooling using this trap mainly looses sodium atoms while potassium thermalizes with the remaining cold sodium cloud. A crucial part for creating a dual species BEC is therefore to trap a large number of cold sodium atoms in the cODT. Furthermore, trapping sodium in general is more efficient than trapping potassium, leading to higher atom numbers in all stages, which enables us to perform RF-induced evaporative cooling ("microwave evaporation") in the magnetic trap on only the sodium atoms, passively cooling potassium via elastic interspecies collisions.

Our strategy for reaching dual species degeneracy is to first optimize the cooling sequence for sodium and afterwards add potassium to the mix and adjust the sequence without changing it dramatically. The first step, the condensation of sodium, has already been achieved using the following cooling stages[1] (also depicted schematically in the upper panel of Figure 4.1):

First, the dark SPOT is loaded for $4\mathrm{s}$ using the 2D MOT as cold atom source. An optical molasses stage is employed to reach temperatures below the Doppler limit before transferring the cloud to a magnetic quadrupole trap.

At this stage, the cODT is turned on directly after the gradient field has been ramped to its highest value. The dipole beams are aligned such that their crossing occurs close to, but not directly at the center of the magnetic trap. This configuration is very similar to the so called "dimple trap" [50], but in our case it additionally prevents Majorana spin-flips [37] by creating a potential well near the problematic region of the magnetic quadrupole trap. We refer to this stage as "hybrid trap".

---

[1] This sequence and its development is described in more detail in the thesis of Jan Kilinc [24].

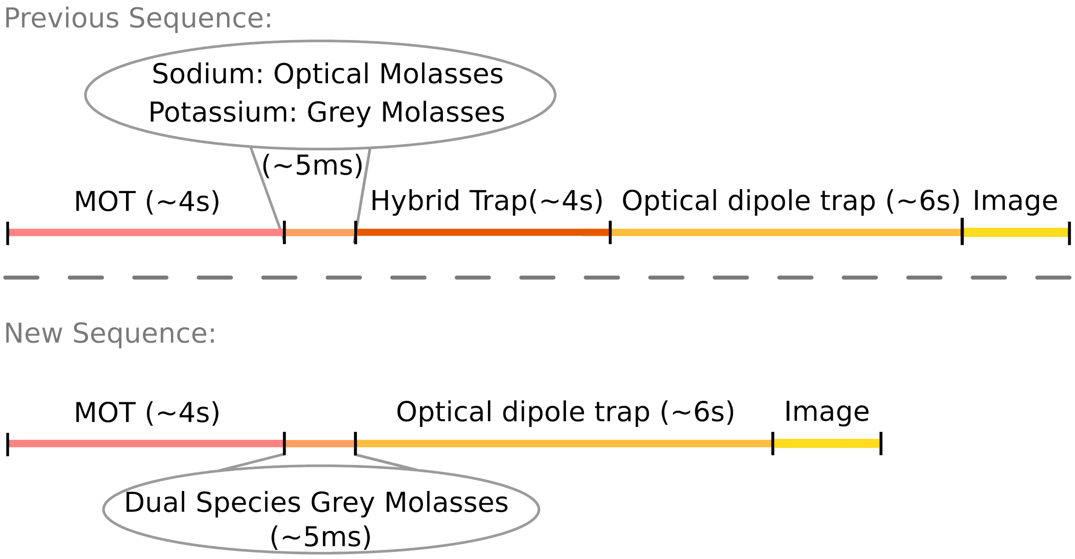
Previous Sequence:
Sodium: Optical Molasses
Potassium: Grey Molasses
(~5ms)
MOT (~4s)
Hybrid Trap(~4s)
Optical dipole trap (~6s)
Image
New Sequence:
MOT (~4s)
Optical dipole trap (~6s)
Image
Dual Species Grey Molasses
(~5ms)

Figure 4.1: Schematic of the previous (upper panel) and the new (lower panel) cooling sequence. Condensation of sodium in single species operation has been achieved with both sequences.

By performing microwave evaporation in the hybrid trap, the amount of atoms trapped in the cODT gradually increases. The last step for reaching condensation is to turn off the gradient field and evaporating in the cODT by gradually lowering the intensities of the trapping beams, allowing atoms with high kinetic energy to spill out[2]. This ultimately reaches the critical PSD for Bose-Einstein-condensation.
Since efficiently cooling sodium is our main priority, the subsequent sections will focus on the operation of the experiment with only sodium unless noted otherwise.

4.2 CHALLENGES INVOLVING THE MAGNETIC TRAP

In this section, I will investigate some of the challenges we faced when trying to optimize the loading of sodium into the magnetic quadrupole trap and the subsequent evaporative cooling. For this purpose I will give a brief overview of the theory behind these techniques. My formulation largely follows [11], which one can refer to for a more in depth discussion of the topic.

Magnetic quadrupole trap: Magnetic trapping is one of the most straight forward methods used by ultra-cold atom experiments, since it can be described completely classically. The potential energy E of an object with magnetic dipole moment $\vec{\mu}$ inside a magentic field $\vec{B}$ is given by

---

[2] For dual species operation, a constant bias field of $110\,\mathrm{G}$ needs to be applied for the evaporative cooling to work. The bias field changes the scattering lengths for particle interactions, which means one can control the elastic scattering rate by changing this field. For sodium, evaporative cooling also works at $0\,\mathrm{G}$.

$$E = -\vec{\mu} \cdot \vec{B}. \tag{13}$$

Since Maxwells equations forbid magnetic fields featuring a global maximum, the only way to locally minimize this term is to have the magnetic dipole oriented anti-parallel to a B-field which contains a local minimum. An example for such a field is a spherical quadrupole field, given by

$$\vec{B} = B'(-x, -y, 2z)^T, \tag{14}$$

where B' is the constant representing the strength of the magnetic gradient. In good approximation such a field can be produced by two coils operated in anti-Helmholtz configuration [24]. In such a field, the torque

$$\vec{\tau} = \vec{\mu} \times \vec{B} \tag{15}$$

will act on the object, eventually aligning its magnetic dipole moment with the field lines and ejecting it from the local minimum. Now, if said object additionally possesses angular momentum anti-parallel to its magnetic dipole moment, this torque will result in a precession of the dipole moment around the magnetic field lines instead, preserving its nearly anti-parallel orientation and thus effectively trapping the object.

With this in mind, one can easily see how a quadrupole field can be used to trap Alkali atoms, since they also possess a permanent magnetic dipole moment as well as non-zero angular momentum. Specifically, the nuclear spin $\vec{I}$ and the total electronic spin $\vec{J}$ couple to the total atomic angular momentum $\vec{F} = \vec{I} + \vec{J}$. For the example of sodium and potassium, which both have $I = 3/2$ and $J = 1/2$ in their ground state, this results in eight magnetic hyperfine states, the energies of which are shown in Figure 4.3 in dependence of the magnetic field strength, where m_f denotes the eigenvalue of the F_z operator. All states with $dE/dB > 0$ will be the ones that can be trapped. In practice we will try to transfer our sodium and potassium clouds to the $|F = 1, m_f = -1\rangle$ state[3] by turning off the repumper for $0.5\mathrm{ms}$ before loading into the quadrupole trap. Without repumping light, atoms in the $|F = 1\rangle$ state won't be transferred back into the cooling cycle and $0.5\mathrm{ms}$ is enough time that most atoms will be off-resonantly excited to the $|F' = 2\rangle$ state from where they can relax to $|F = 1\rangle$. Since all Zeeman levels of the $|F = 1\rangle$ state are populated equally, we loose 2/3 of the atoms during

---

[3] This is due to unfavorable spin-changing collisions involving atoms in the $|F = 2, m_f = 1\rangle$ state. Selectively trapping atoms in the $|F = 2, m_f = -2\rangle$ state would also work, but this requires a more complicated sequence [24].

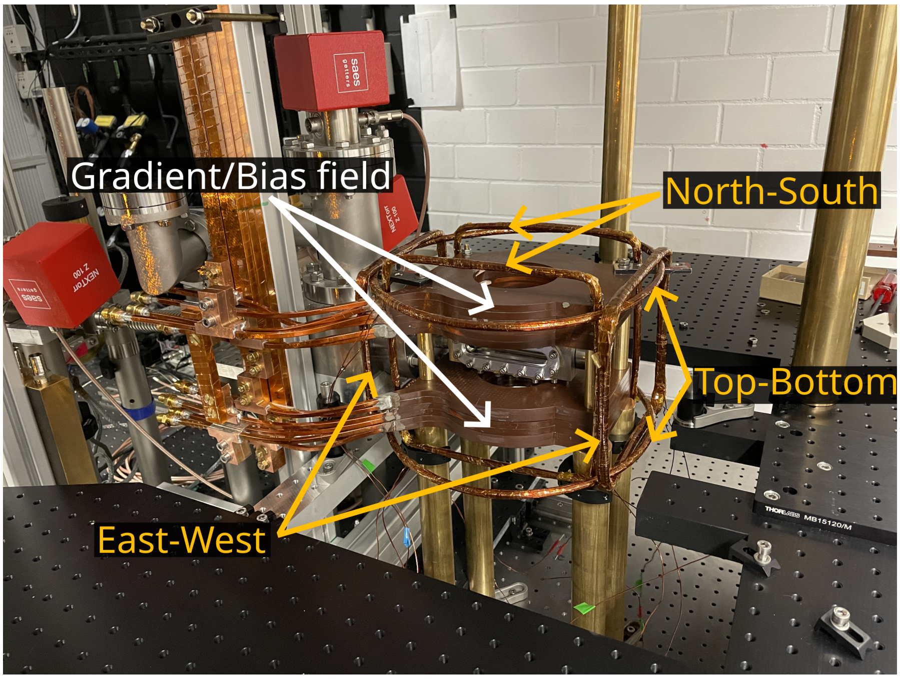

Figure 4.2: Picture of the magnetic field coils. The large pair of coils (white) is used for generating a quadrupole field of up to $300\,\mathrm{G\,cm^{-1}}$ and the bias field for tuning particle interactions. The offset coils (yellow) are used to zero the magnetic field inside the chamber, counteracting any stray magnetic fields that might be present in the lab (e.g. the magnetic field of the earth).

the transfer of the magnetic trap.
In the SoPa, the gradient field is generated by a pair of large copper coils situated above and below the science chamber. A picture of the setup is shown in Figure 4.2. These coils are hollow to allow for water to be pumped through them during operation to facilitate cooling. An H-bridge makes it possible to switch the current direction of one of the coils to go from anti-Helmholtz to Helmholtz configuration [24]. In this configuration a constant bias fields can be generated, which is used to tune the particle scattering lengths via Feshbach resonances during the cODT. To counteract any stray magnetic fields that might be present in the laboratory, three additional pairs of coils are employed ("offset" coils), operated in Helmholtz-configuration. They are also depicted in Figure 4.2.

Forced microwave evaporation: The principle of evaporative cooling is to eject atoms with relatively high velocities from the trap, effectively lowering the average kinetic energy of the ensemble, which is equivalent to lowering its temperature. When done correctly, the atoms leaving the trap also remove entropy from the system, which leads to an increase in phase space density. For this to work efficiently one needs to ensure a high elastic collision rate inside the trap, such that the ensemble quickly reaches thermal equilibrium after discarding some fast atoms. This collision rate depends on the scattering length we have seen in Chapter 1.

In a magnetic trap, evaporative cooling of sodium atoms can be achieved by driving hyperfine transitions between the trapped $|F = 1, m_f = -1\rangle$ and the untrapped $|F = 2, m_f = -2\rangle$ state. As one can see in Figure 4.3, the frequency required for this transition changes with different magnetic field strengths. The atoms are constantly moving inside the magnetic trap and the more kinetic energy they possess, the larger is their biggest possible distance from the trap center. Subsequently, atoms with higher kinetic energy will experience higher magnetic fields, which makes it possible to resonantly excite the $|F = 1, m_f = -1\rangle \rightarrow |F = 2, m_f = -2\rangle$ transition for fast atoms using microwaves, while not addressing slower ones. By linearly ramping the frequency of the microwave towards the zero field resonance (around $1771\mathrm{MHz}$ for sodium), one can continuously remove the hottest atoms from the magnetic trap until the previously mentioned Majorana losses become strong enough to prevent any further increase in phase space density ([37], [11]).
Historically, this technique has proven to be very effective to efficiently cool an atom cloud, for example the creation of the first sodium BEC, which was also one of the first successful attempts to produce a BEC in general, utilized evaporative cooling in a magnetic trap [10]. This is why we employ it in our experiment as well to cool sodium atoms. The microwave frequency ramp we currently use in our cooling sequence is $3.5\mathrm{s}$ long, starts at $1620\mathrm{MHz}$ and ends at $1762.5\mathrm{MHz}$.

4.2.1 *Sloshing in the magnetic trap*

While optimizing timing parameters of the magnetic trap[4] in an effort to increase the atom number of the sodium BEC, we noticed that the shape of the atomic cloud was changing a lot over time. An example for this "sloshing" of the sample can be seen in Figure 4.4. This indicates that the center of the magnetic trap is not well aligned with the MOT and molasses stages, which could have unwanted effects like heating and thus higher atom loss rates. We were able to suppress this sloshing by either increasing the duration of the ramp of the magnetic field from $50\mathrm{ms}$ to $450\mathrm{ms}$ or by decreasing the end value of the ramp, which results in a shallower trap[5]. Both of these observations support the hypothesis of poor mode matching, since they both decrease the amount

---

[4] Specifically how fast we increase or decrease the gradient at the start and at the end of the magnetic trap, as well as how long we hold the sodium cloud in the trap before commencing the microwave evaporation.

[5] The configuration where the sloshing was observed had a gradient of $300\mathrm{G\,cm^{-1}}$, at a gradient of $100\mathrm{G\,cm^{-1}}$ the sloshing was completely suppressed.

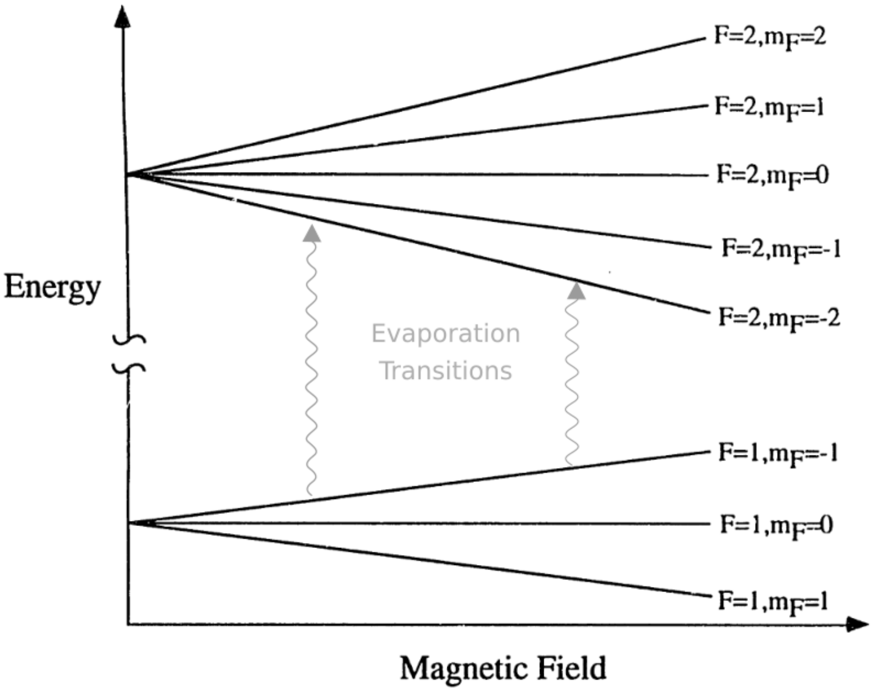
Energy
F=2,m$_F$=2
F=2,m$_F$=1
F=2,m$_F$=0
F=2,m$_F$=-1
F=2,m$_F$=-2
Evaporation Transitions
F=1,m$_F$=-1
F=1,m$_F$=0
F=1,m$_F$=1
Magnetic Field

Figure 4.3: Energy levels of the hyperfine states of an alkali atom in the ground state as a function of magnetic field strength for low magnetic fields (at high magnetic fields the Pashen-Back-effect becomes relevant, where the energy dependence seizes to be linear, see [41]). The transition we utilize for the microwave evaporation is indicated with grey arrows, the different lengths correspond to different resonant frequencies when varying the magentic field strength (Figure adapted from [11]).

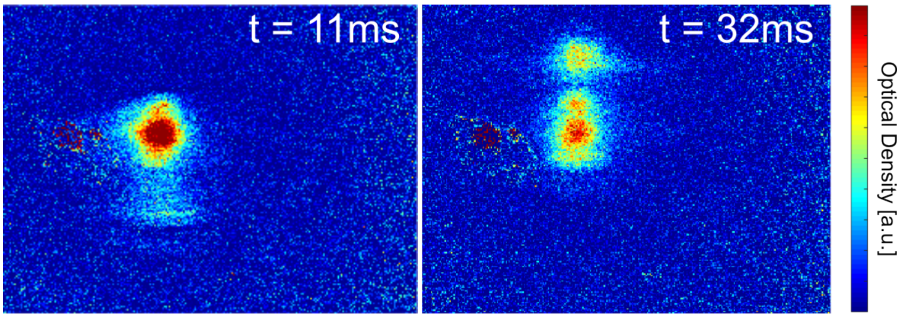

Figure 4.4: Absorption images illustrating the "sloshing" in the magnetic quadrupole trap. Both pictures where produced using the same sequence, the only difference is different hold times in the trap (indicated by their labels). The dark spot on the left of the atom cloud is caused by the scratch in the viewport that was mentioned in Section 3.3.

of acceleration the cloud experiences during the loading process, thus the amplitude of the sloshing is diminished.

Further investigation then revealed that in pictures with very low TOF of $100\mu s$ taken after the magnetic trap, the peak atomic density is shifted multiple millimeters with respect to the maximum seen in the MOT with the same TOF. Since the MOT also requires a magnetic field minimum to operate and its performance seemed reasonable, this observation could indicate that there is a constant magnetic field present in the science chamber, which would explain the positional shift as follows: Given a magnetic gradient field as in Equation 14 together with a constant offset field B_0, the magnetic field $B(x)$ is given by (for simplicity only in x-direction)

$$B(x) = B_0 + B'x. \tag{16}$$

As I have explained above, the potential minimum for alkali atoms in the low field seeking $|F = 1, m_f = -1\rangle$-state will be located at $|B(x)| = 0$. Subsequently, setting Equation 16 to zero and solving for x gives us the position of the potential minimum as a function of the offset field and the strength of the gradient:

$$x(B_0, B')\big|_{B=0} = \frac{-B_0}{B'} \tag{17}$$

This equation shows that the potential minimum for the MOT and the magnetic trap can change drastically if $B_0 \neq 0$, due to the large difference[6] of the gradient B', which could explain the poor mode matching we observed. The absence of any constant magnetic fields is also important for grey molasses cooling (see Section 4.4.4), so calibrating the offset coils such that $B_0 = 0$ is essential for moving forward.

---

[6] The MOT is usually operated with a gradient of $10\,\mathrm{G\,cm^{-1}}$, while the magnetic trap uses $300\,\mathrm{G\,cm^{-1}}$.

4.2.2 *Offset Coil Calibration*

For zeroing the magnetic fields we can make use of very similar concepts as we have seen above: If there is a magnetic field present, the degeneracy of the hyperfine states is lifted, from which follows that the resonant frequencies of different hyperfine transitions can be distinguished as well. This can be visualized by exposing the atoms to different microwave frequencies while they are trapped inside a purely optical trap[7]. As explained before, the atoms are prepared in the $|F = 1, m_f = -1\rangle$-state, so there are 3 relevant transitions:

$$\begin{aligned} |F = 1, m_f = -1\rangle &\to |F = 2, m_f = 0\rangle \\ |F = 1, m_f = -1\rangle &\to |F = 2, m_f = -1\rangle \\ |F = 1, m_f = -1\rangle &\to |F = 2, m_f = -2\rangle \end{aligned}$$

Before taking an absorption image, we pulse the resonant cooling light from the imaging path, which will excite the atoms in the $F = 2$ state, removing them from the trap. Therefore, if the microwave frequency is resonant to a hyperfine transition, a significant loss of atoms in the trap can be observed in the final image. When scanning the microwave frequency that is applied at the end of each sequence while $B_0 \neq 0$, we should observe 3 distinct minima in atom number, the separation of which (in frequency space) are directly correlated to the strength of the magnetic field present in the system. Now, one can simply vary the current running through the offset coils in an effort to minimize the distance between the minima until they eventually overlap, at which point B_0 should be zero. This method is called *microwave spectroscopy*, a more detailed description of our approach can be found in [24] together with the results for our experiment.

After calibrating the magnetic fields this way we still observed the same unwanted dynamics in the magnetic trap that we have seen before. To cross check the results of this calibration procedure, a second technique was employed, where we tried to measure the $1/B'$-dependence of the magnetic traps position Equation 17 for different currents passing through the offset coils. Unfortunately, this investigation had to end early, since it started shortly before we discovered the issues with the sodium oven and viewports described in Figure 3.2.3. Due to these more urgent matters, we did not pursue this topic further, however, we performed a similar measurement with the new setup for

---

[7] We use our cODT for this purpose, which is at the very end of our current sequence, see Section 4.1.

	Top-Bottom coil	East-West coil	North-South coil
Current $[\mathrm{A}]$	0.35	-0.025	0
Field $[\mathrm{G}]$	0.57	-0.05	0

Table 4.1: Results of microwave spectroscopy for zeroing the magnetic field in the science chamber using the offset coils. The coils are named by their orientation within the lab (the "East-West" coil pair is arranged along the fine imaging beam, see also Figure 4.2). The calibration factor from current to field can be found in [24].

our offset coils, which will be the topic of the next section.

4.2.3 *Upgrade of the power supplies for the offset coils*

While it can be an issue that the magnetic trap position depends on offset fields, this fact can be used to our advantage: The loading process from the magnetic trap into the dipole trap can be augmented by ramping the offset coils during the hybrid trap. Optimizing this on atom number in the dipole trap should result in the optimal balance between trap overlap and minimal Majorana losses. During this optimization process, we noticed that we are limited by the direction of the offset coil currents, since the results from the microwave spectroscopy suggested rather small currents as optimal parameters for the MOT and molasses stages. This meant that the position of the trap center could only be shifted significantly by *increasing* the currents, so we were only able to effectively move in one direction with each pair of coils. To overcome these limitations, Helmut Strobel and Pirmin Adam designed and built a circuit which enables bidirectional operation the offset coils during a sequence[8]. After the issues with the oven were temporarily solved, the old power supplies where augmented by the new circuit and we again performed microwave spectroscopy for calibration purposes. The results are presented in Table 4.1. The offset fields are similar in magnitude as the values from previous calibrations (see [24]), however during this measurement it was not possible to overlap all three dips in atom number perfectly, i.e. there was still a offset magnetic field left. This probably results from limitations of the newly implemented circuit, where small changes in control voltage do not properly translate to changes in the supplied current. A new version of this circuit is currently in development, where this issue will be resolved.

Calibrating the offset coils by utilizing the position of the magnetic trap has the advantage that one doesn't require having signal in the dipole trap nor a setup for generating strong microwave pulses. As a proof of concept, we tried performing this calibration for the vertical coil pair. For this, the magnetic trap was loaded with sodium using the dark SPOT with a subsequent grey molasses stage[9], where the strength of the magnetic field gradient is varied from shot to shot from around $300\mathrm{G\,cm^{-1}}$ down to $20\mathrm{G\,cm^{-1}}$. Since the dark SPOT and the grey molasses were optimized with a certain configuration for the offset coils, this configuration is used up until after the grey molasses stage. We ramp to the offset field of interest during the loading process into the magnetic trap.

---

[8] More details on the circuit can be found in Appendix A.

Performing a linear fit to the trap position over $1/B'$ reveals if there is a residual field left in the vertical direction, i.e. it shows whether $B_{0,z} = 0$ or not. We repeat this scan using different currents for the vertical offset coil pair with the goal of minimizing the slope of the linear fit. The results of these measurements are shown in Figure 4.5. We can see that when extrapolating the linear fits they converge at around $3.15\mathrm{mm}$ for $1/B' = 0$, i.e. infinitely strong gradient, with a maximum distance between two fits being roughly $25\mathrm{\mu m}$ in this point. Also one can observe the slope of the fit changing for different currents, with $B_{offset,z} = -2.27\mathrm{G}$ being the smallest slope so far.

The result from this measurement do not agree well with the results of the microwave spectroscopy presented in Table 4.1. Since the grey molasses is reaching the expected temperatures for both species (see upcoming sections) using the offset field values determined by microwave spectroscopy, it is likely that the results from that calibration method are correct, since a magnetic offset field would inhibit the functionality of the grey molasses cooling scheme. It is likely that there are systematic errors in the measurement shown in Figure 4.5 that have not been properly understood yet. For example, the change in offset fields during the loading of the magnetic trap could introduce sloshing, altering the measured trap position. Another systematic shift could arise from the choice of the fit function used to extract the position of the atomic cloud. Here, a gaussian fit was performed on the atomic density distribution integrated along the x-axis, however, the shape of an atomic cloud in a magnetic quadrupole trap is not well described by a gaussian for high gradients and low TOFs. This could possibly be avoided by a slower ramping of the currents, as described in Section 4.2.1. Lastly, it is possible that the strong magnetic fields of the quadrupole trap could magnetize metallic parts on the table, also influencing the measurement.

Until now, this measurement was only performed in the z-direction, since it is the only coil pair which shifts the trap position solely perpendicular to the axis of the coarse imaging. Changing the currents of the other two offset coil pairs can result in movement of the trap position which is parallel to this axis. Such a movement would not be visible in the resulting absorption image. In order to capture the change in trap position along the xy-direction, one would require an additional vertical

---

[9] see Section 4.4.2.

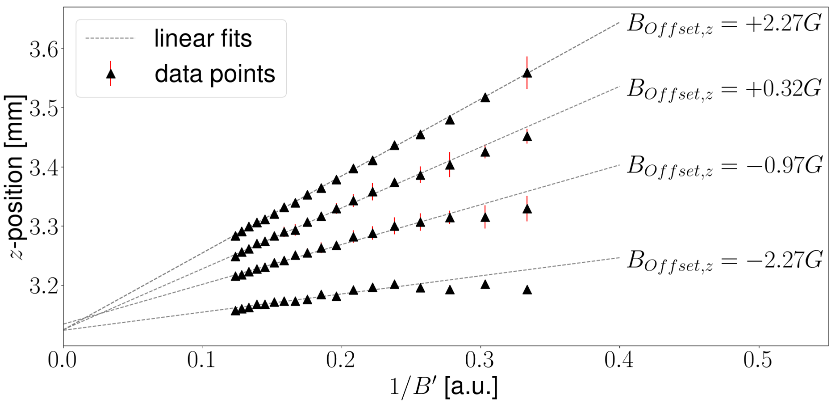

Figure 4.5: z-position of the sodium atom cloud in the magnetic trap as a function of one over the magnitude of the magnetic field gradient. Each data point (black triangles) represents the mean position in four individual absorption images with the same settings. The vertical position was extracted from the absorption image by a two-dimensional gaussian fit. The measurement was repeated for different currents running through the vertical coil pair, for each setting a linear fit was performed (grey dashed lines). The trap position is given relative to the top edge of the absorption image.

imaging system.

4.3 OPTIMIZING THE CROSSED OPTICAL DIPOLE TRAP (CODT)

4.3.1 *Dipole laser setup*

The cODT is a central part of our system and, crucially, the stage were we want to reach quantum degeneracy. Properly aligning the two dipole beams such that they cross each other exactly at their focus is therefore critical. A schematic of the cODT-setup we use in our experiment is shown in Figure 4.6. For initial aligment of each beam with the atom cloud, we use a beam of resonant sodium light that is passed through the last mirror of the dipole beam path. The coating of this mirror ensures good reflection only in the $1030 - 1090\mathrm{nm}$ range, which allows good transmission of the $589\mathrm{nm}$ light. We now load the sodium 3D MOT and align the beam to the atomic cloud[10], while keeping the beam as horizontal as possible by using a laser level and a ruler. We start with around $10\mathrm{mW}$ of sodium light. After optimizing the alignment (i.e. maximizing the disturbance of the MOT), we decrease the power of the resonant light such that we have barely enough power to destroy the atomic cloud. Next, we increase the current running through the

---

[10] When the beam hits the MOT one can clearly see how the resonant light disturbs the florescence and shape of the atomic cloud.

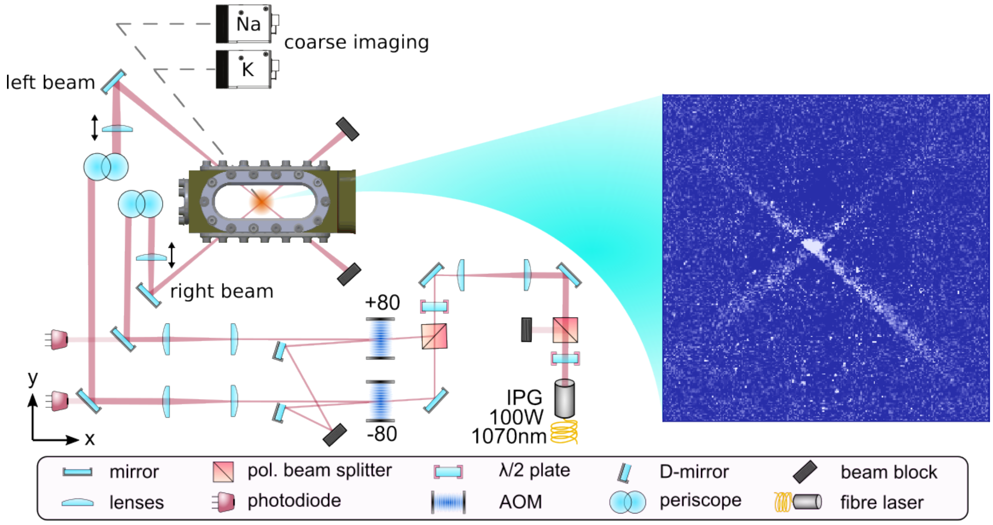

Figure 4.6: Illustration of our optical layout for the cODT. AOMs in conjunction with photodiodes are employed for power stabilization, the AOM-frequencies are noted in units of MHz. The beams are focused into the science chamber using $f = 400\mathrm{mm}$ lenses, which are mounted on linear translation stages for adjusting the focus position. The position of the low resolution absorption imaging is illustrated by the grey dashed line. In the picture to the right, the florescence of sodium atoms in the cODT was captured with a camera above the science chamber pointed downwards. Figure adapted from [24].

gradient coils, effectively compressing the MOT and adjust the alignment again. These steps are then iterated a few times before the dipole beam is turned on and the sodium beam and the IR laser beam are overlapped using the last two mirrors of the dipole beam laser path.

After doing this for both beams we use the low resolution horizontal absorption imaging to take pictures after the hybrid trap with low TOF, where the atoms trapped in the beams are clearly visible. We expect to see a large difference in how each beam looks on these images, since the camera is looking into the science chamber at an angle which is almost parallel one of the dipole beams, while the other beam is basically perpendicular to this (see Figure 4.6). Now we can easily overlap the beams using this signal and then switch to the high resolution imaging to do fine adjustments by optimizing the atom number in the trap. At this stage we also tried to adjust the focus of each beam by using the linear translation stages on which the lenses are mounted, again optimizing for highest atom number. Adjusting the focus of the left beam lead to an increase in atom number of roughly 10%. For the right beam, no improvements could be made.

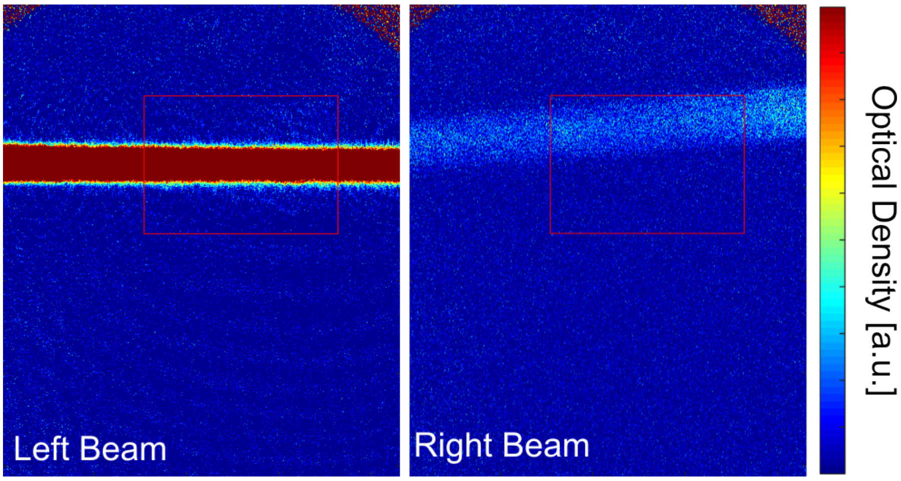

Figure 4.7: Asymmetry of atom number in single dipole beams. Pictures were taken at the end of the hybrid trap with a TOF of $100\mu s$ using the high resolution horizontal absorption imaging.

4.3.2 *Asymmetry of the Dipole beams*

While optimizing the sodium-BEC-sequence we noticed a stark asymmetry in the optical density of sodium atoms between the two dipole beams when we only turn on one of them at a time (see Figure 4.7). Not only that, we also observed an angle in the right beam, although they seemed to be parallel when aligning them initially, which was ensured by measuring the beam height after the last mirror and at the beam block at the end of the beam path[11]. In contrast to the lower resolution imaging, the high resolution imaging is situated directly on one of the horizontal symmetry axes of the cODT, which is why we would expect very similar looking beams both in angle and atom number.
In an effort to equalize both sides, we tried to adjust the position of the beam with lower atom number, but it did not seem possible to improve it. Afterwards we coarsely changed the position of the focus by moving the lens on its translation stage, which has 2.5cm of travel. This required realigning the beam as described above and also didn't help in achieving symmetry.

Since the angle of the right beam on the pictures persisted even after realigning all of the imaging system (which was performed because we noticed a lot of clipping of the imaging beam), we determined that the angle is an artifact of the imaging system itself. One hypothesis was that the objective is not perfectly situated in the horizontal plane with the cODT, which would introduce a symmetric angle for both beams in the image. This is illustrated in Figure 4.8: If the beam crossing is observed perfectly from the side (upper panel of Figure 4.8) there should be no visible angle between the beams, in any other case, an angle will be observed. In addition to this, something along the imaging path could cause the final image to rotate[12], which, by pure chance, lets one beam appear as straight, while the other one has twice the angle introduced by the imperfect alignment to the horizontal plane.

---

[11] We calculated that the angle visible in the picture should correspond to roughly 10cm beam height difference between the last mirror and the beam block. We measured no height difference at all with an accuracy of a few millimeters.

The last part can be checked by determining the direction of gravity in the image, which we originally assumed to be parallel to the images y-axis. To confirm this, we can use the sodium BEC sequence and simply let the condensate fall and take pictures at different TOFs, fitting a parabolic trajectory to the condensate position afterwards. Jan Kilinc already reported the results of such an experiment in his thesis [24], but here it was utilized to measure the magnification of the fine imaging system and it was assumed that gravity points straight down. I revisited this data and noticed that there is a component of gravity pointing in the x-direction of the image, which is shown in Figure 4.9. The fit results[13] imply that the y-axis of the image (z-direction on the table) is rotated relative to gravity by roughly $2.3°$.

Using this information, I overlapped the two images from Figure 4.7, rotated them such that gravity is actually pointing downwards and then compared the relative angles of the beams to the horizontal plane. The results of this are presented in Figure 4.10. The angle of the beams with respect to the experimental table (which is perpendicular to gravity) can be calculated by digitally measuring the lengths of the white dashed lines and applying basic trigonometry. The result is that both beams have a similar angle of $\alpha \approx \beta \approx 3.1°$ to the x-axis of the coordinate system defined by gravity. This confirms the hypothesis that the visible angle is not caused by misalignment of the dipole beams, but by imperfect alignment of the imaging system[14] and the apparent asymmetry in the angles of the beams is the result of a $2.3°$ rotation of the image with respect to gravity.

Furthermore, the magnification also needs to be recalculated, since the condensate traversed a larger distance than what was previously thought. The effect is very small however, since the angle is quite shallow. The corrected magnification for the fine imaging system comes out to be $M_{fine} = 20.38(3)$, which is within the error of the originally calculated value $M_{fine} = 20.36(3)$ [24].

---

[12] E.g. the camera itself or the sensors within the camera could be rotated with respect to the laboratory coordinate system

[13] For simplicity, we use a 2D gaussian as fit function, which is not quite accurate, since the density distribution of the condensate is, in theory, parabolic [24]. However, since the distribution is symmetric and we are only interested in the peak position, the result should not be influenced by this.

[14] I.e. the situation in our experiment is similar to what is shown schematically in the lower panel of Figure 4.8.

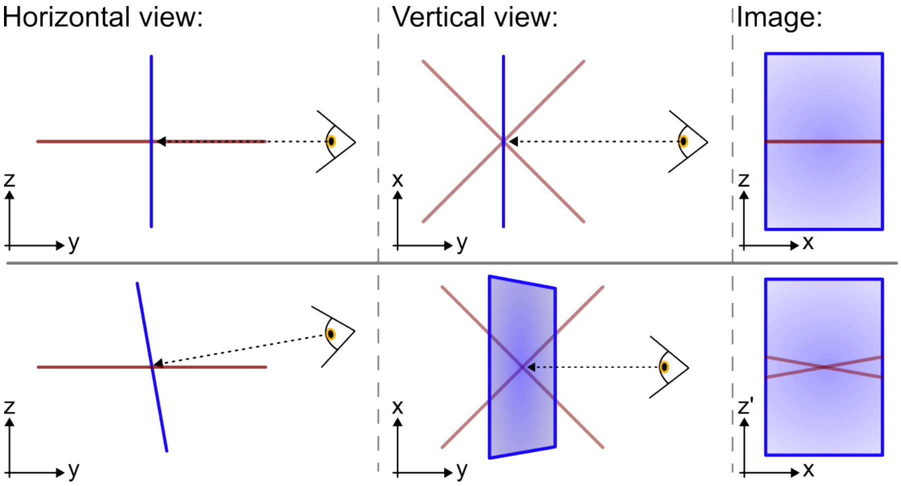

Figure 4.8: Visualization of the effect of a vertical offset of the imaging system with respect to the cODT. The red lines represent the dipole beams, the blue lines/squares represent the imaging plane. In the upper panel, the observer views the system along the horizontal plane defined by the two dipole beams, resulting in both beams being overlapped in the imaging plane. In the lower panel, an angle is introduced, causing the imaging plane to be tilted. Due to this, a projection of the angle between the dipole beams is visible in the final image.

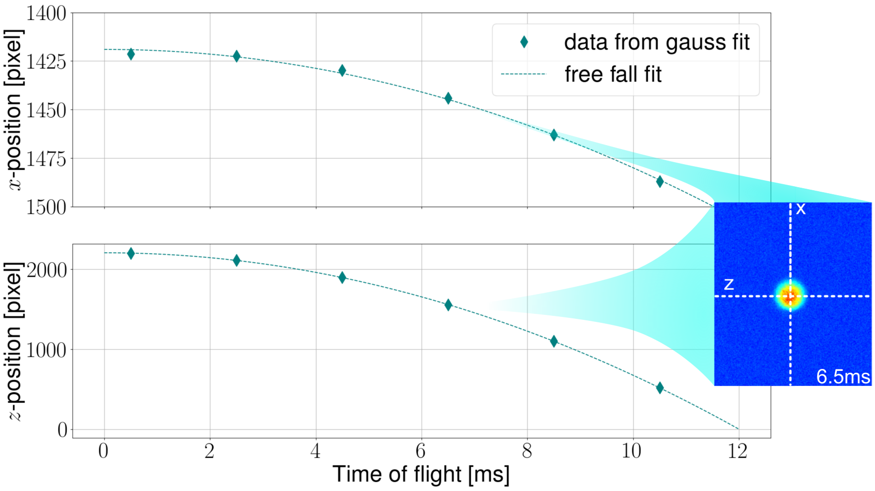

Figure 4.9: Trajectory of a falling condensate on the absorption imaging. The dotted lines represent the fit of the trajectory assuming a constant force. The inset shows an example for a density distribution of the condensate, to which a 2D Gaussian is fitted to extract the x and z-position of the cloud.

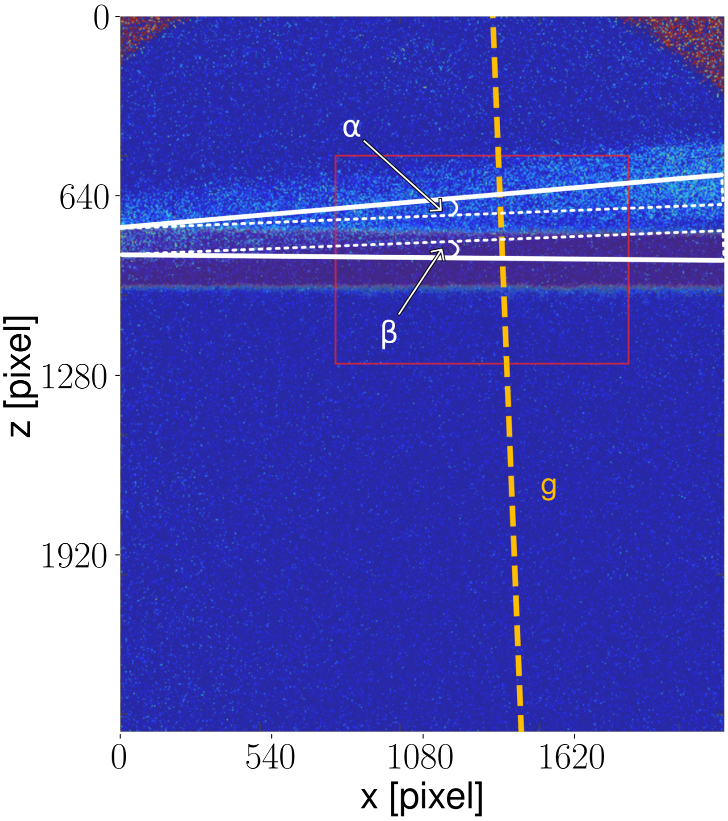

Figure 4.10: Visualization of the angles between the beams and gravity (yellow dashed line labeled "g") in the imaging plane. The white dashed lines are perpendicular to gravity, while the continuous white lines mark the middle of each beam. The resulting triangle can be used to calculate the angles α and β. The background consists of the overlapped pictures from Figure 4.7 (the beams do not cross in this figure, since the pictures were taken with non-optimal alignment of the cODT).

The second problem of asymmetry was the difference in optical density of the atomic clouds trapped in the two beams. It persists to this day, however not as prominent as in Figure 4.7. We think that it is connected to the focus not being in the correct spot for the beam that is less dense, since the atom number in the cODT is not very sensitive to movement of the last lenses translation stage for this beam, while it is very sensitive to the same changes in the other beam path. This is still an ongoing investigation.

4.4 OUR COOLING SEQUENCE: THEN AND NOW.

4.4.1 *Adding Potassium*

The sequence described in Section 4.1 works well when looking at only sodium, with up to $6 \cdot 10^4$ atoms in the resulting condensate. However, until now we were not able to use a similar sequence to achieve dual species quantum degeneracy. Due to light-assisted heteronuclear collisions the potassium atom number in the dual species MOT is already lower [36], which has an observable effect on all subsequent stages. For potassium, a grey molasses cooling scheme was implemented (see Section 4.4.4), which is performed during the molasses stage of the sodium cooling sequence. Despite the grey molasses reaching a temperature of $11 \mu\mathrm{K}$, we observed that the transfer into the magnetic trap is very inefficient for potassium: less than 10% of the atoms present in the grey molasses seem to be trapped here, whereas the expected ratio should be around $1/3$, as mentioned before. The atom number of sodium in the magnetic trap does not seem to be affected by the presence of potassium.

Our hypothesis is that the strong magnetic field gradient needed for an efficient microwave evaporation causes the scattering length for K-K and Na-K collisions to be unfavorable in large portions of the trap, since a sodium-potassium mixture exhibits a rich spectrum of Feshbach resonances (see Figure 1.1). This is supported by our observations of the cODT during the microwave evaporation. Here, the sodium atomic density is strongly limited if potassium is simultaneously trapped, even though we do not see additional losses for sodium during the magnetic trap.

For these reasons, we eventually decided to restructure our cooling approach for sodium to make the sequence more suitable for capturing potassium and sodium atoms simultaneously. The main goal for the new sequence was shortening the magnetic trap or omitting it entirely. To achieve this, the microwave evaporation and the molasses stage are replaced by a D_1 grey molasses for Sodium, necessitating a restructuring of our laser system, so it can supply light stabilized on the D_1 and D_2 lines of sodium (see Section 3.1.1).

4.4.2 *Sodium Grey Molasses*

As discussed above, the plan for the new sequence is to eliminate the reliance on the magnetic trap to achieve a high PSD in the dipole trap in an effort to reduce unfavorable Na-K-collisions. Therefore, we want to achieve as little atom loss as possible from the MOT-stage to the grey molasses stage, while reaching a temperature of around $10\mathrm{K}$. In the new sequence (depicted in the lower panel of Figure 4.1), we again utilize the dark SPOT, which is loaded for $4\mathrm{s}$, directly followed by the grey molasses, for which the D_2-light is shuttered and the D_1-light is turned on for $2.1\mathrm{ms}$. During the the next $2.6\mathrm{ms}$, both frequencies of the Raman-transition are ramped towards higher detuning Δ, while the intensities are lowered to ensure efficient cooling [24]. After the grey molasses, the cODT is activated. The scattering lengths in our system at $0\mathrm{G}$ also cause unfavorable collisions, which is why a constant bias field needs to be applied during the cODT[15]. Since the grey molasses requires $0\mathrm{G}$, this field needs to be ramped up to $110\mathrm{G}$ directly after the grey molasses is finished. At this field strength, the interactions between the trapped atoms allow for evaporative cooling by lowering the intensities of the dipole beams.

For the grey molasses to work it is crucial that the two frequencies of the D_1-light fulfill the Raman-condition. To ensure this is the case, we can scan the frequency of the EOM. We have seen in Section 2.4 that we can measure temperature by measuring the width of the atomic cloud at different TOFs. This in turn also means that the width of the cloud can be used as a relative estimator of the temperature when scanning other parameters with fixed TOF[16], for example the EOM-frequency. The results of such a measurement are shown in Figure 4.11, where we looked for the Raman-condition using a TOF of $12\mathrm{ms}$. A clear dip in width is visible at $1771.6\mathrm{MHz}$, while the atom number stayed mostly constant[17].

As mentioned before, the design and implementation of the sodium D_1-molasses was the project of Malaika Göritz. For the optimization procedure and results of various measurements for characterizing the functionality of the cooling scheme, the reader can refer to her masters thesis [16]. Figure 4.11 is mainly presented as a proof that the current setup is working as intended.

With the new sequence, it is possible to produce a sodium BEC in

---

[15] This bias field is created by switching the direction of current for one of magnetic gradient field coils, going from an anti-Helmholtz to a Helmholtz configuration.

[16] One has to be careful to not look at the width of the cloud in isolation. The atom number is also important, since background noise could introduce systematic errors to the Gauss fits for low atom numbers. This could lead to higher width for smaller atom numbers, even when the temperature is the same.

[17] The standard deviation on the atom number in Figure 4.11 is relatively big, since we had a lot of issues with the consistency of our sequence during the time of this measurement, probably due to instabilities in laboratory temperature and laser power, see Chapter 5.

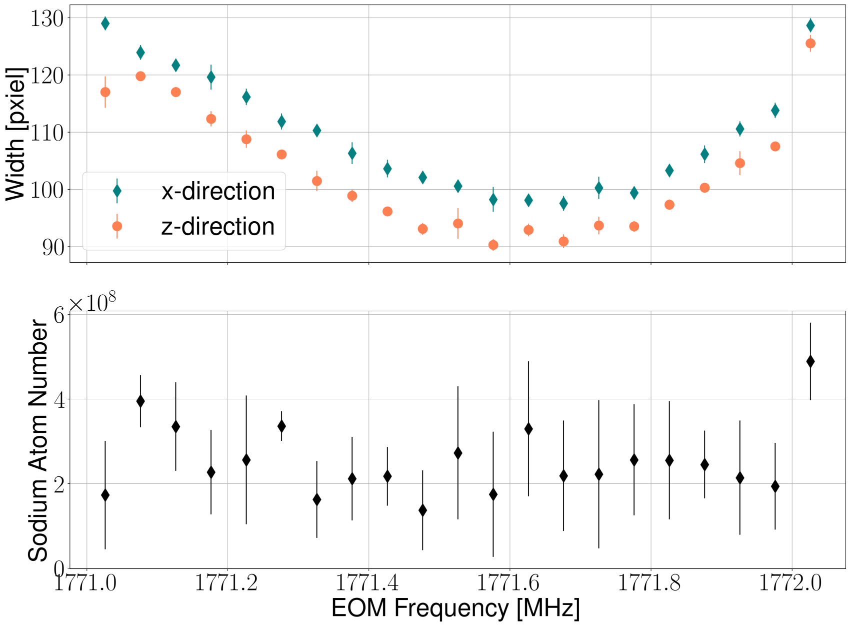

Figure 4.11: Scan of EOM-frequency used to produce the repumper-sidebands for the sodium grey molasses. Each point is the average of three measurements using exactly the same sequence. The upper panel shows the width of the density distribution of trapped atoms after $12\mathrm{ms}$ TOF, which has been extracted by a Gauss fit to the integrated signal for each axis. In the lower panel, the average atom number is plotted for the corresponding data points in the upper panel.

single species operation, however, it still lacks consistency, since the condensation only happens occasionally and the resulting condensate is fairly small. This inconsistency is most likely related to general instability issues of the experiment that have not been resolved yet.

4.4.3 *Re-optimization of Potassium*

Due to the challenges we faced with the sodium oven and the overall strategy to first focus on creating a sequence that reliably produces a sodium BEC, the potassium system was not in use for multiple successive months. Since we were eager to test the new setup in dual species operation, I mainly focused on re-optimizing large parts of the potassium system during the restructuring of the sodium laser system. The first step in this endeavor was to ensure a sufficient output of all the TA modules as explained in Section 3.1.4. Afterwards we focused on aligning the 2D and 3D MOTs: Each beam was checked for proper circular polarization, sufficient power and good beam balancing. It was ensured that all the beams were overlapped with their respective counter-propagating beam. For finding the initial 2D MOT alignment, we used a CMOS-camera[18], which is located behind the potassium 2D MOT chamber and points into the push-beam viewport, which is located where the 2D MOT beams cross in the center of the chamber. Through all the steps described in this section and by setting the MOT AOMs to values that have worked previously, we were able to obtain a signal (a faint fluorescing cloud on the camera) by adjusting the offset of the laser lock while monitoring the video of the camera. We optimized this signal by adjusting the frequencies of the AOMs until we were able to trap potassium atoms in the 3D MOT, from which point on we utilized the optimization procedure described in Section 3.2.2.

After this, we started optimizing the 3D MOT: in the first step, we again optimized AOM frequencies on atom number by using the absorption imaging. Then, we slightly modulated the magnetic field gradient sinusoidally using a signal generator, which in turn modulates the strength of the position dependent term of the scattering force. With this, the atom cloud expands and contracts alongside the magnetic field modulation. By adjusting the beam alignment and balancing, we aimed for fully symmetric expansion and contraction of the cloud, to ensure equal radiation forces in all directions. After this last step we started again with the optimization of the 2D MOT and iterated through all subsequent steps until no further improvements were visible.

4.4.4 *Potassium Grey Molasses*

Like for the sodium grey molasses, the potassium grey molasses' aim is to minimize temperature while capturing the maximal amount of atoms in the dipole trap. To optimize this, we first try to find the configuration for which the Raman-condition is fulfilled by ramping the AOM-frequencies for both D_1-AOMs, where we ensure that we start with both frequencies blue-detuned at least 5Γ to their respective transition. Afterwards, we scan Δ at the start and the end of the grey molasses, optimizing mainly for temperature, since atom numbers are not affected significantly by these scans.

The result of this optimization is shown in Figure 4.12. The left plot shows a temperature measurement as discussed in Section 2.4. The fits yield results of $T_{cloud,x} = 11\mu\mathrm{K}$ in x-direction and $T_{cloud,z} = 19\mu\mathrm{K}$ in z-direction. As indicated by the red circle, this measurement was taken at the optimal detunings for the Raman-condition, which can be seen in the right plot. The data was taken after all previously described optimization steps. To the right of the minimum in the left panel we see a strong increase in width (i.e. temperature), which happens due to single-photon-transitions being shifted closer to resonance. This causes heating, because the light is blue-detuned and thus has the opposite effect as an optical molasses.

---

[18] *Allied Vision Mako G-030 B*, same model that is used in the coarse imaging setup.

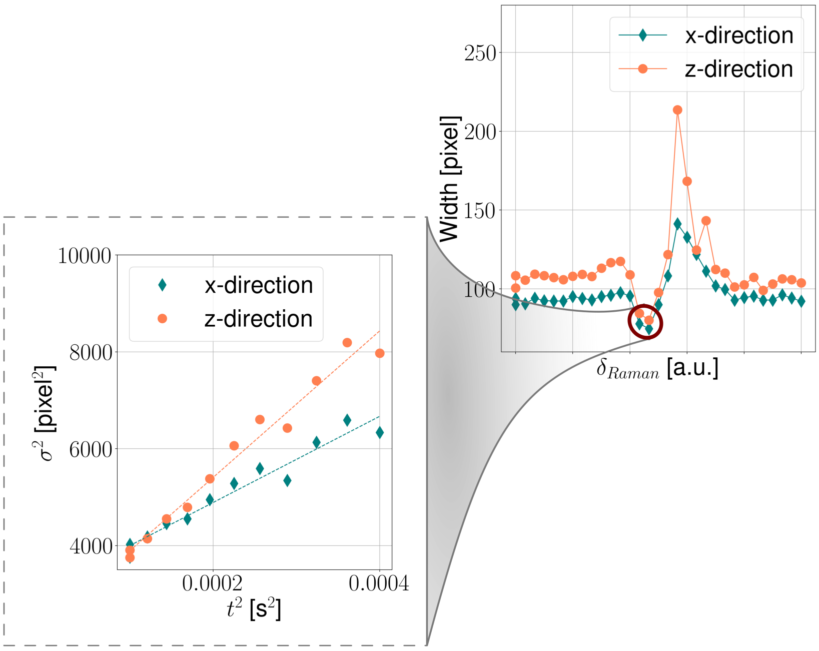

Figure 4.12: Measurements relevant for the grey molasses cooling of potassium. On the right, we scanned the AOM-frequencies with a relatively long TOF of $12\mathrm{ms}$ to find the configuration which fulfills the Raman-condition. Similar to the procedure for sodium, the width of the atom cloud after the TOF can be used as a relative estimator for the temperature. The data shows a clear minimum in width, which is where a quantitative measurement of the temperature was performed by utilizing the ballistic expansion of the cloud (see Section 2.4). This measurement is shown in the right plot with the linear fits plotted as dashed lines in the respective color for x and z direction. The measured temperatures are $T_{cloud,x} = 11\mu\mathrm{K}$ and $T_{cloud,z} = 19\mu\mathrm{K}$.

4.4.5 *Dual Species Operation*

With the grey molasses now implemented for both species, the question is if this change would improve the dual species operation significantly. During the first trials with the updated sequence, we were able to capture $^{23}\mathrm{Na}$ and $^{39}\mathrm{K}$ atoms simultaneously in the dipole trap, which is shown in Figure 4.13. This measurement serves as a first proof of concept for our new cooling approach, even though the amount of trapped atoms was not high enough to reach the critical PSD for condensation after performing evaporative cooling in the cODT. It is worth noting that the crossing of the dipole beams is not visible for sodium. This is due to the high optical density along a large portion of the dipole beams for sodium, which makes it impossible to distinguish the crossing point from the single beams.

Unfortunately, the high resolution imaging system for potassium was not operational at the time of taking these measurements, which is why only qualitative data could be taken using the low resolution imaging system[19]. Before we were able to fix the high resolution imaging, the ion pump of the potassium 2D MOT chamber registered a exponentially increasing ion pump current, which lead us to believe that there was a leak in the vacuum. To properly search for the leak, we needed to access the viewports of this vacuum chamber. For this, it was necessary to move multiple optics of the potassium 2D MOT, inhibiting the operation of the potassium 3D MOT and all subsequent steps.

In the end, the rise in ion pump current was determined to stem from so called *leakage current*, an effect where conducting depositions[20] can build up on the ion pump electrodes over time, increasing the current without the pressure inside the chamber actually being higher. Details on this issue are described in [20]. Up until now, the potassium 2D MOT has not been realigned, which makes further investigations of dual species operation impossible.

---

[19] The cODT is only a few pixels in diameter on this camera, which makes a quantitative measurement of atom number very unreliable.

[20] Most likely potassium-depositions.

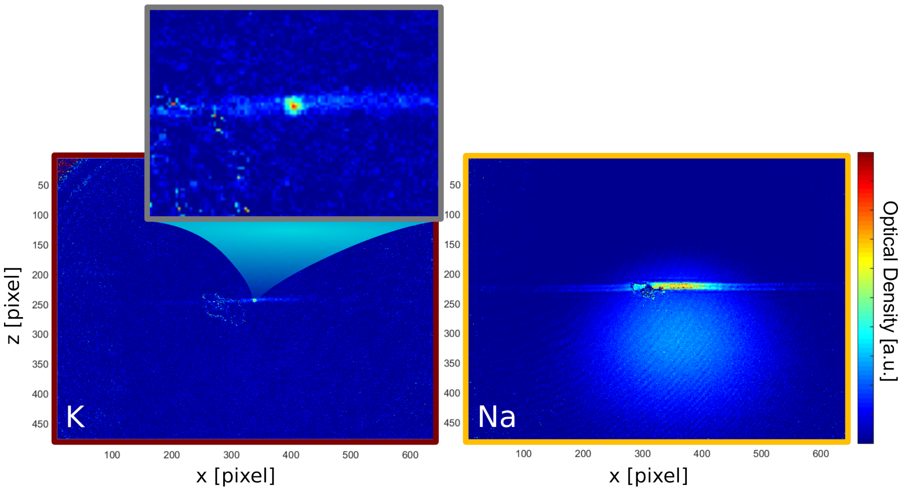

Figure 4.13: Picture of both species trapped in the same cODT with a TOF of 100µs (potassium on the left and sodium on the right). This measurement was taken by using a sequence without the magnetic trap, instead utilizing the dual species grey molasses cooling. For sodium, a cloud of atoms that did not get trapped in the cODT is still visible in the background.

5

OUTLOOK AND CONCLUSION

5.1 WHAT THE FUTURE HOLDS

The newly implemented sodium grey molasses and the altered cooling sequence already produced promising, but still preliminary results when it comes to trapping both species in the cODT simultaneously. However, there is still a lot of work to be done before being able to perform analog quantum simulations.

The upcoming steps towards this goal are realizing two large projects for which the planning phase and large parts of the preparation have already been finished. The first is a new optical dipole trap, which will be used to make our BEC quasi two-dimensional. A picture of its setup is shown in Figure 5.1. This trap will be especially useful for e.g. investigating domain formation as described in Section 1.2. At the point of writing this, we already implemented all necessary components and observed a signal that suggests that we were able to load this trap with sodium atoms, however, this investigation is still ongoing.

The second project is an additional high resolution imaging system in the vertical direction, which will be used as main detection device for the 2D-dual-species-BEC. The implementation of this will probably be postponed until we are able to consistently produce a two species condensate. A detailed account of the preparation and characterization for both projects can be found in Lilo Höcker's PhD thesis [20].

Unfortunately, various issues arose quite recently, which prevent further efforts to improve the signal of the 2D optical dipole trap or to continue dual species operation. For example, the potassium 2D MOT currently isn't in an operational state. Furthermore, the vacuum of the sodium 2D MOT also had a leak not long ago, which, at the time of writing this, still hinders any work on improving the cooling sequence, even in single species operation. On top of this, we have faced major instability issues over the last several months, where atom numbers in the sodium 3D MOT change by a factor of 2 to 3 in the span of minutes[1]. This causes a lot of inconsistencies when trying to perform quantitative measurements or while optimizing parts of the sequence, since it is hard to distinguish if the decrease or increase in atom number is caused by a deliberate change of something that is currently investigated or by fluctuations of some other part of the

---

[1] A hint of this instability can be seen in the lower panel of Figure 4.11, where a high standard deviation for the atom numbers can be observed, even though the whole measurement only took around 10 minutes.

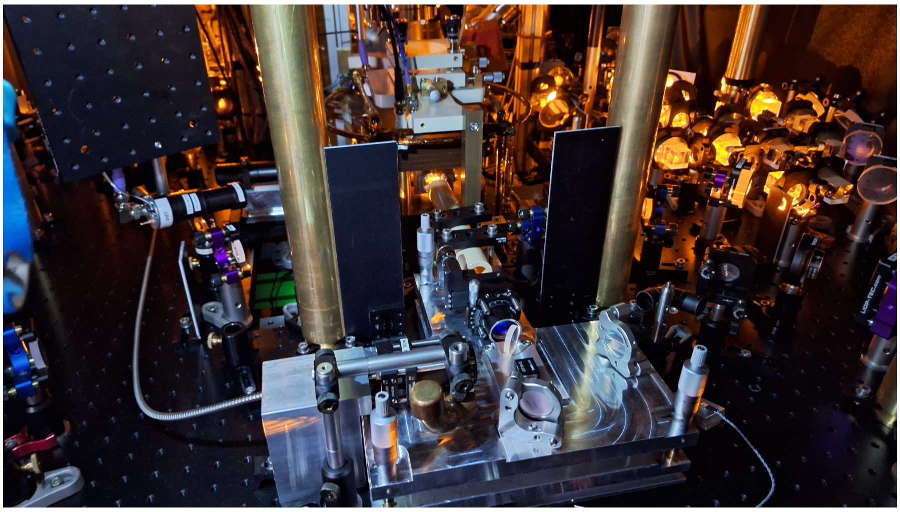

Figure 5.1: Picture of the 2D optical dipole trap setup on the experiment table.

experiment. Fixing these instability issues will therefore be crucial for moving forward.

5.2 CONCLUSION

In this thesis, I have presented an overview of the SoPa, a new $^{23}\mathrm{Na}$-$^{39}\mathrm{K}$ mixture experiment and described many of the challenges we were faced with during the past year, ranging from issues with the atom sources, the optimization and characterization of a TA setup and various topics connected to the improvement of our cooling sequence and measuring process.
In summary, this thesis mirrors the everyday life of a experimental physicist working in an ultra cold atom lab. It highlights the vast complexity of such a project and how every part of the whole apparatus is prone to malfunction at some point, requiring constant scrutiny regarding every important component. The fact that we are a mixture laboratory only adds to this complexity.
Even though it can be frustrating when new challenges arise before previous ones could be solved, the best way to move forward is to solve one problem at a time. This work shows that progress is definitely not linear, but usually still tends towards the envisioned goal.

Appendices

A

BIDIRECTIONAL POWER SUPPLY

Figure A.1 shows the circuit that makes it possible to run current through the offset coils in both directions, switching during the sequence if necessary. A voltage divider ensures that $1\mathrm{V}$ of control voltage corresponds to $1\mathrm{A}$ of current running through the coils. At its core, the circuit works by employing an OpAmp together with two transistors. Depending on the sign of the control voltage on the OpAmp, one of the transistors will supply current to the coil. They are positioned in a way that the direction of current changes depending on which transistor supplies it.

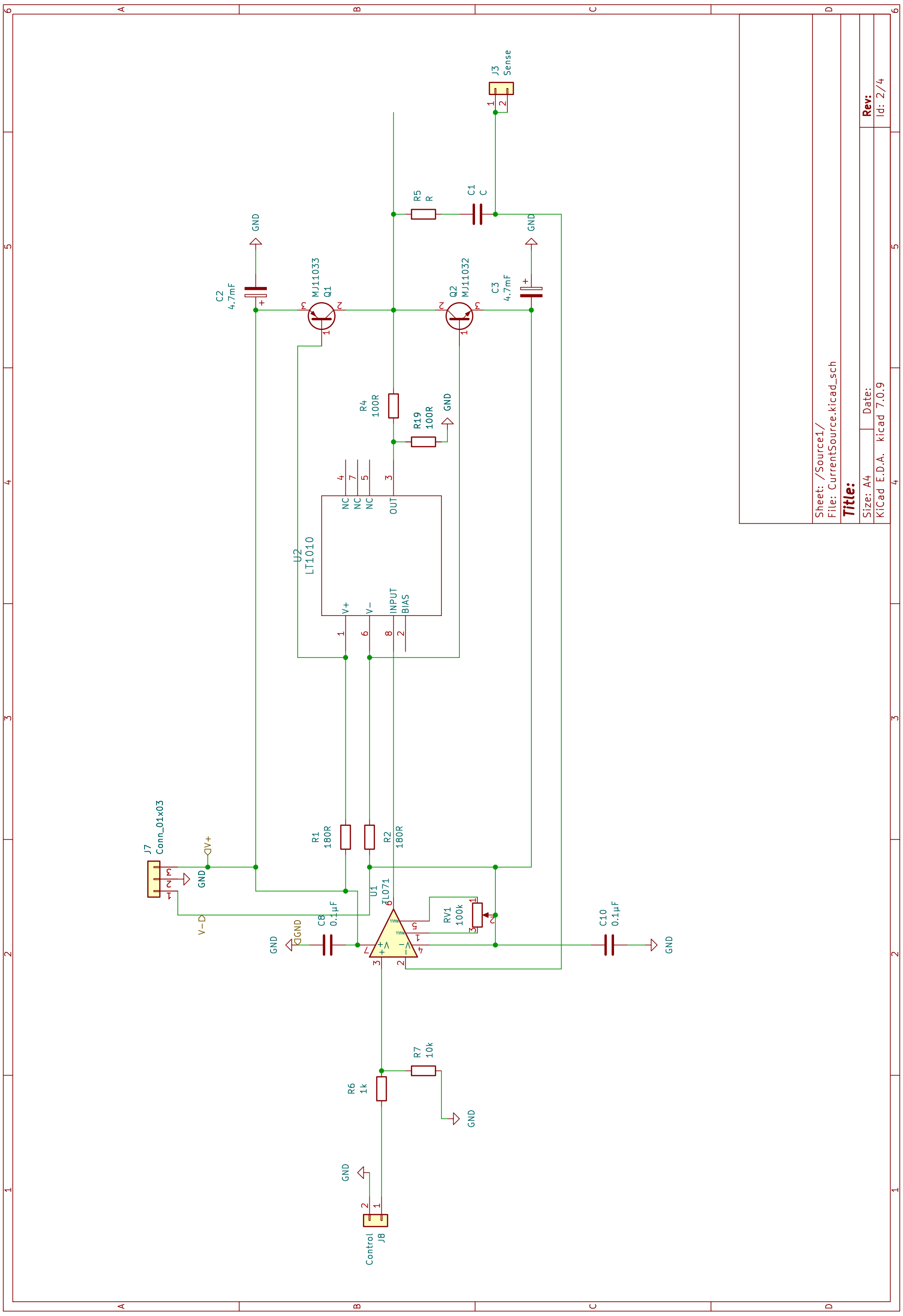
J3
Sense
R5
R
C1
C
GND
C2
4.7mF
MJ11033
Q1
Q2
MJ11032
C3
4.7mF
R4
100R
R19
100R
U2
LT1010
NC
NC
NC
OUT
V+
V-
INPUT
BIAS
J7
Conn_01x03
V+
V-
R1
180R
R2
180R
U1
TL071
C8
0.1µF
RV1
100k
C10
0.1µF
R7
10k
R6
1k
Control
J8
Sheet: /Source1/
File: CurrentSource.kicad_sch
Title:
Size: A4
Date:
KiCad E.D.A. kicad 7.0.9
Rev:
Id: 2/4

Figure A.1: Circuit used for bidirectional operation of the offset coils (designed by Pirmin Adam and Helmut Strobel).

LIST OF ACRONYMS

MOT	Magneto Optical Trap
TA	Tapered Amplifier
SPOT	Spontaneous-force Optical Trap
cODT	crossed optical dipole trap
BEC	Bose-Einstein-Condensate
ASE	Amplified Spontaneous Emission
TOF	Time Of Flight
UHV	Ultra High Vacuum
AOM	Acousto Optical Modulator
EOM	Electro Optic Modulator
VSCPT	Velocity-selective Coherent Population Trapping
PBS	Polarizing Beam Splitter
PSD	Phase Space Density
CO	crossover

LIST OF FIGURES

Figure 1.1 Scattering lengths of ^{23}Na and ^{39}K (a_{Na} and a_K respectively) and interspecies scattering length (a_{NaK}) as a function of bias field strength (both species are in the $|F=1, m_f=-1\rangle$ state.). The relation between scattering length and coupling strength is given in Equation 5. The miscibility parameter $\delta_g(B)$ is plotted in the inset. Figure taken from [38]. 4

Figure 2.1 One dimensional schematic illustration of the mechanism of a MOT. The B-field switches directions at $z=0$ and the counter-propagating MOT-beams with the frequency of $f=\omega/2\pi$ have opposite circular polarization. This results in a force pointing towards the center of the coordinate system, because of the position dependent energy of different M_J states. Figure adapted from [12]. 8

Figure 2.2 Illustration of the grey molasses cooling mechanism. (Upper panel) The level scheme of the λ-type system is plotted with the two required laser frequencies in Raman-condition and the detuning Δ. (Lower Panel) The system is simultaneously irradiated with two counter-propagating beams containing both aforementioned frequencies. Their polarizations are in "lin $\perp$ lin"-configuration, resulting in a polarization gradient. This gradient gives rise to a position-dependent energy of the bright state $|b\rangle$ in the dressed state picture, while the dark state $|d\rangle$ stays unmodulated. The probability of atoms in the dark state coupling to the bright state is highest in the potential minimum. The movement of the atom causes it to convert kinetic energy to potential energy ("climbing the hill") before being excited and falling back down to the dark state. Figure adapted from [47]. . . . 11

Figure 3.1 Energy level schemes for the atoms used in our experiment (A: $^{23}\mathrm{Na}$, B: $^{39}\mathrm{K}$). The transitions utilized in our cooling sequence are denoted by colored arrows, the frequency shifts from the hyperfine structure are written in brackets in units of MHz (distances are not to scale). The values for sodium were taken from [42], the potassium values from [43]. The figure itself was largely adapted from [24]. 14
Figure 3.2 Spectroscopy signal from saturated absorption spectroscopy registered by the photodiode for the D_1 lock and the error signal generated from it. The lockpoint is marked by a dashed line. The data was taken using an oscilloscope. The spectroscopy signal was shifted downward by $0.33\mathrm{V}$ and then scaled by a factor of 50 to improve its visibility in this plot. The visible peaks correspond to the following transitions (from left to right): $|F=2\rangle \rightarrow |F'=2\rangle$, $|F=2\rangle \rightarrow |F'=1,2\rangle$ (CO) and $|F=2\rangle \rightarrow |F'=1\rangle$. 15
Figure 3.3 Schematic illustration of the sodium spectroscopy setup. Both beams enter the spectroscopy cell in opposite directions and are retroreflected by "D"-shaped mirrors to not obstruct the respective other beam. A PBS together with a $\lambda/4$-plate is used to guide the beam onto a fast photodiode after passing the cell twice. 16
Figure 3.4 Overview of the AOM quadruple pass used to generate sodium repumper light. A prism mirror is employed to introduce a vertical offset to the first order of the first pass, making two additional passes possible by retro-reflection of the second pass using a "D"-shaped mirror. Figure adapted from [24]. 17
Figure 3.5 Overview of the sodium laser table containing all AOM-paths and EOMs (rotated for space reasons). The AOM- and EOM-frequencies are noted in Table 3.1. Figure adapted from [16]. . . 19
Figure 3.6 Optical layout of the sodium-D_1-setup. The AOM is used to shift Δ, the EOM generates the repumper sideband. A Fabry-Pérot-Interferometer is employed to monitor the intensity of the repumper. Figure adapted from [16]. 20
Figure 3.7 Sketch of the geometry of a TA diode (from [23]). 21
Figure 3.8 Illustrations of a TA module used in our experiment 22

Figure 3.9 Setup on laser table to generate light necessary for cooling and imaging potassium (rotated for space reasons, figure adapted from [24]). . . . 23
Figure 3.10 (Upper panel) Measurement result for the output power of the 2D MOT TA over the applied current. The seed power for this measurement was $11.6\mathrm{mW}$, which corresponds to the seed power during regular operation of the experiment. (Lower panel) Coupling efficiency of light amplified by the TA. 25
Figure 3.11 Example of the output beam spectrum of the 2D MOT TA acquired using a Fabry-Pérot-Interferometer and an oscilloscope. The middle peak corresponds to the cooling light, the peak to the right corresponds to the repumper. 25
Figure 3.12 (Upper panel) Measurements of the 2D MOT TAs output power dependence on the power ratio of cooler and repumper light in the seed beam. Each data point represents the mean of 20 separate Fabry-Pérot-Spectra for the same setting. The red bars represent the standard deviation. (Lower panel) Relative fluctuations of the ratios seen in the upper panel to estimate the stability of each setting. 28
Figure 3.13 Illustration of the vacuum system, viewed from the top. The housings of the ovens are located below the respective 2D MOT chambers (not visible in this picture). The red cubes are ion-getter pumps (Model: *SAES NEXTorr Z100/D500*). 30
Figure 3.14 Example for the signal we use to optimize the 2D MOTs. The trigger signal is used to periodically open a mechanical shutter, which blocks the 3D MOT beams when closed. A photodiode is used to measure the florescence of the 3D MOT (the potassium 3D MOT in this case). The signal can be viewed with an oscilloscope (which was also utilized to capture this data). The trigger signal was scaled down by a factor of 150 for visibility reasons. 31
Figure 3.15 Picture of the sodium depositions on the push beam viewport, which is currently not heated. The lower viewports looked very similar before heating them. The "clear" spot is where the push beam usually enters the chamber, it seems that the sodium depositions are suppressed here. . 32

Figure 3.16 Pictures taken looking through the slower viewport for different temperatures of the lower viewports. One can clearly see the florescence increasing with the higher temperatures. The visible sodium deposits are marked with red circles. 35

Figure 3.17 Ion pump currents from all three pumps during the time when we first started heating the lower viewports. The first dotted grey line marks the start of the heating process, which is direcly followed by a rise of ion pump current in the sodium 2D MOT chamber. The second grey dotted line marks the point where the temperature of the viewports exceeded the melting point of sodium, which is $97.8°\mathrm{C}$. This also caused a spike in measured the ion pump current. 35

Figure 3.18 Overview of the two imaging systems used for measurements of the density distributions of trapped atoms. The coarse imaging uses a single lens and lokks at the science chamber with an angle, such that the imaging beam is almost parallel one of the horizontal MOT-beam-pair. The fine imaging is aligned to be symmetric to the MOT-beams and uses two lenses to facilitate higher magnification. The imaging beams for sodium and potassium are overlapped directly after the fiber coupler using dichroic mirrors. Right before the camera, another dichroic mirror splits the beams apart and guides them toward their respective cameras. The figure was adapted from [24]. 37

Figure 4.1 Schematic of the previous (upper panel) and the new (lower panel) cooling sequence. Condensation of sodium in single species operation has been achieved with both sequences. 40

Figure 4.2 Picture of the magnetic field coils. The large pair of coils (white) is used for generating a quadrupole field of up to $300\,\mathrm{G\,cm^{-1}}$ and the bias field for tuning particle interactions. The offset coils (yellow) are used to zero the magnetic field inside the chamber, counteracting any stray magnetic fields that might be present in the lab (e.g. the magnetic field of the earth). 42

Figure 4.3 Energy levels of the hyperfine states of an alkali atom in the ground state as a function of magnetic field strength for low magnetic fields (at high magnetic fields the Pashen-Back-effect becomes relevant, where the energy dependence seizes to be linear, see [41]). The transition we utilize for the microwave evaporation is indicated with grey arrows, the different lengths correspond to different resonant frequencies when varying the magentic field strength (Figure adapted from [11]). 44
Figure 4.4 Absorption images illustrating the "sloshing" in the magnetic quadrupole trap. Both pictures where produced using the same sequence, the only difference is different hold times in the trap (indicated by their labels). The dark spot on the left of the atom cloud is caused by the scratch in the viewport that was mentioned in Section 3.3. 45
Figure 4.5 z-position of the sodium atom cloud in the magnetic trap as a function of one over the magnitude of the magnetic field gradient. Each data point (black triangles) represents the mean position in four individual absorption images with the same settings. The vertical position was extracted from the absorption image by a two-dimensional gaussian fit. The measurement was repeated for different currents running through the vertical coil pair, for each setting a linear fit was performed (grey dashed lines). The trap position is given relative to the top edge of the absorption image. 49
Figure 4.6 Illustration of our optical layout for the cODT. AOMs in conjunction with photodiodes are employed for power stabilization, the AOM-frequencies are noted in units of MHz. The beams are focused into the science chamber using $f = 400\mathrm{mm}$ lenses, which are mounted on linear translation stages for adjusting the focus position. The position of the low resolution absorption imaging is illustrated by the grey dashed line. In the picture to the right, the florescence of sodium atoms in the cODT was captured with a camera above the science chamber pointed downwards. Figure adapted from [24]. 50

Figure 4.7 Asymmetry of atom number in single dipole beams. Pictures were taken at the end of the hybrid trap with a TOF of $100\mu s$ using the high resolution horizontal absorption imaging. 51

Figure 4.8 Visualization of the effect of a vertical offset of the imaging system with respect to the cODT. The red lines represent the dipole beams, the blue lines/squares represent the imaging plane. In the upper panel, the observer views the system along the horizontal plane defined by the two dipole beams, resulting in both beams being overlapped in the imaging plane. In the lower panel, an angle is introduced, causing the imaging plane to be tilted. Due to this, a projection of the angle between the dipole beams is visible in the final image. 53

Figure 4.9 Trajectory of a falling condensate on the absorption imaging. The dotted lines represent the fit of the trajectory assuming a constant force. The inset shows an example for a density distribution of the condensate, to which a 2D Gaussian is fitted to extract the x and z-position of the cloud. 53

Figure 4.10 Visualization of the angles between the beams and gravity (yellow dashed line labeled "g") in the imaging plane. The white dashed lines are perpendicular to gravity, while the continuous white lines mark the middle of each beam. The resulting triangle can be used to calculate the angles α and β. The background consists of the overlapped pictures from Figure 4.7 (the beams do not cross in this figure, since the pictures were taken with non-optimal alignment of the cODT). 54

Figure 4.11 Scan of EOM-frequency used to produce the repumper-sidebands for the sodium grey molasses. Each point is the average of three measurements using exactly the same sequence. The upper panel shows the width of the density distribution of trapped atoms after 12ms TOF, which has been extracted by a Gauss fit to the integrated signal for each axis. In the lower panel, the average atom number is plotted for the corresponding data points in the upper panel. 57

Figure 4.12 Measurements relevant for the grey molasses cooling of potassium. On the right, we scanned the AOM-frequencies with a relatively long TOF of 12ms to find the configuration which fulfills the Raman-condition. Similar to the procedure for sodium, the width of the atom cloud after the TOF can be used as a relative estimator for the temperature. The data shows a clear minimum in width, which is where a quantitative measurement of the temperature was performed by utilizing the ballistic expansion of the cloud (see Section 2.4). This measurement is shown in the right plot with the linear fits plotted as dashed lines in the respective color for x and z direction. The measured temperatures are $T_{cloud,x} = 11\mu\text{K}$ and $T_{cloud,z} = 19\mu\text{K}$. 59
Figure 4.13 Picture of both species trapped in the same cODT with a TOF of $100\mu\text{s}$ (potassium on the left and sodium on the right). This measurement was taken by using a sequence without the magnetic trap, instead utilizing the dual species grey molasses cooling. For sodium, a cloud of atoms that did not get trapped in the cODT is still visible in the background. 61
Figure 5.1 Picture of the 2D optical dipole trap setup on the experiment table. 64
Figure A.1 Circuit used for bidirectional operation of the offset coils (designed by Pirmin Adam and Helmut Strobel). 68

[1] M. H. Anderson, J. R. Ensher, M. R. Matthews, C. E. Wieman, and E. A. Cornell. “Observation of Bose-Einstein Condensation in a Dilute Atomic Vapor.” In: *Science* 269.5221 (July 14, 1995). Publisher: American Association for the Advancement of Science, pp. 198–201. DOI: `10.1126/science.269.5221.198`. URL: `https://www.science.org/doi/10.1126/science.269.5221.198`.

[2] A. Aspect, E. Arimondo, R. Kaiser, N. Vansteenkiste, and C. Cohen-Tannoudji. “Laser Cooling below the One-Photon Recoil Energy by Velocity-Selective Coherent Population Trapping.” In: *Physical Review Letters* 61.7 (Aug. 15, 1988). Publisher: American Physical Society, pp. 826–829. DOI: `10.1103/PhysRevLett.61.826`. URL: `https://link.aps.org/doi/10.1103/PhysRevLett.61.826`.

[3] Cosetta Baroni, Giacomo Lamporesi, and Matteo Zaccanti. *Quantum Mixtures of Ultracold Atomic Gases*. May 23, 2024. DOI: `10.48550/arXiv.2405.14562`. arXiv: `2405.14562[cond-mat,physics:quant-ph]`. URL: `http://arxiv.org/abs/2405.14562`.

[4] Immanuel Bloch, Jean Dalibard, and Sylvain Nascimbène. “Quantum simulations with ultracold quantum gases.” In: *Nature Physics* 8.4 (Apr. 2012). Publisher: Nature Publishing Group, pp. 267–276. ISSN: 1745-2481. DOI: `10.1038/nphys2259`. URL: `https://www.nature.com/articles/nphys2259`.

[5] N Bogolubov. “ON THE THEORY OF SUPERFLUIDITY.” In: *Journal of Physics* X1.1 (1947).

[6] Cheng Chin, Rudolf Grimm, Paul Julienne, and Eite Tiesinga. “Feshbach resonances in ultracold gases.” In: *Reviews of Modern Physics* 82.2 (Apr. 29, 2010). Publisher: American Physical Society, pp. 1225–1286. DOI: `10.1103/RevModPhys.82.1225`. URL: `https://link.aps.org/doi/10.1103/RevModPhys.82.1225`.

[7] Steven Chu, J. E. Bjorkholm, A. Ashkin, and A. Cable. “Experimental Observation of Optically Trapped Atoms.” In: *Physical Review Letters* 57.3 (July 21, 1986). Publisher: American Physical Society, pp. 314–317. DOI: `10.1103/PhysRevLett.57.314`. URL: `https://link.aps.org/doi/10.1103/PhysRevLett.57.314`.

[8] Giacomo Colzi, Gianmaria Durastante, Eleonora Fava, Simone Serafini, Giacomo Lamporesi, and Gabriele Ferrari. “Sub-Doppler cooling of sodium atoms in gray molasses.” In: *Physical Review A* 93.2 (Feb. 18, 2016), p. 023421. ISSN: 2469-9926, 2469-9934. DOI: `10.1103/PhysRevA.93.023421`. URL: `https://link.aps.org/doi/10.1103/PhysRevA.93.023421`.

[9] J. Dalibard and C. Cohen-Tannoudji. "Laser cooling below the Doppler limit by polarization gradients: simple theoretical models." In: *JOSA B* 6.11 (Nov. 1, 1989). Publisher: Optica Publishing Group, pp. 2023–2045. ISSN: 1520-8540. DOI: `10.1364/JOSAB.6.002023`. URL: `https://opg.optica.org/josab/abstract.cfm?uri=josab-6-11-2023`.

[10] K. B. Davis, M. O. Mewes, M. R. Andrews, N. J. van Druten, D. S. Durfee, D. M. Kurn, and W. Ketterle. "Bose-Einstein Condensation in a Gas of Sodium Atoms." In: *Physical Review Letters* 75.22 (Nov. 27, 1995). Publisher: American Physical Society, pp. 3969–3973. DOI: `10.1103/PhysRevLett.75.3969`. URL: `https://link.aps.org/doi/10.1103/PhysRevLett.75.3969`.

[11] Kendall B. Davis, Marc-Oliver Mewes, Michael A. Joffe, Michael R. Andrews, and Wolfgang Ketterle. "Evaporative Cooling of Sodium Atoms." In: *Physical Review Letters* 74.26 (June 26, 1995). Publisher: American Physical Society, pp. 5202–5205. DOI: `10.1103/PhysRevLett.74.5202`. URL: `https://link.aps.org/doi/10.1103/PhysRevLett.74.5202`.

[12] C. J. Foot. *Atomic Physics*. Oxford University Press, 2005. 346 pp. ISBN: 978-0-19-850695-9.

[13] I. M. Georgescu, S. Ashhab, and Franco Nori. "Quantum Simulation." In: *Reviews of Modern Physics* 86.1 (Mar. 10, 2014), pp. 153–185. ISSN: 0034-6861, 1539-0756. DOI: `10.1103/RevModPhys.86.153`. arXiv: `1308.6253[cond-mat,physics:quant-ph]`. URL: `http://arxiv.org/abs/1308.6253`.

[14] E. P. Gross. "Structure of a quantized vortex in boson systems." In: *Il Nuovo Cimento (1955-1965)* 20.3 (May 1, 1961), pp. 454–477. ISSN: 1827-6121. DOI: `10.1007/BF02731494`. URL: `https://doi.org/10.1007/BF02731494`.

[15] Emmanuel Mercado Gutierrez, Gustavo Alves de Oliveira, Kilvia Mayre Farias, Vanderlei Salvador Bagnato, and Patricia Christina Marques Castilho. "Miscibility Regimes in a 23Na–39K Quantum Mixture." In: *Applied Sciences* 11.19 (Jan. 2021). Number: 19 Publisher: Multidisciplinary Digital Publishing Institute, p. 9099. ISSN: 2076-3417. DOI: `10.3390/app11199099`. URL: `https://www.mdpi.com/2076-3417/11/19/9099`.

[16] Malaika Göritz. "Masterthesis." Supervisor: Markus Oberthaler. PhD thesis. Hedielberg University.

[17] Lorenz Hahn. "Setup of a Tapered Amplifier Unit for Application in an Ultracold Mixture Experiment." Bachelor Thesis.

[18] Maurus Hans, Finn Schmutte, Celia Viermann, Nikolas Liebster, Marius Sparn, Markus K. Oberthaler, and Helmut Strobel. "High signal to noise absorption imaging of alkali atoms at moderate magnetic fields." In: *Review of Scientific Instruments* 92.2 (Feb. 1,

2021), p. 023203. ISSN: 0034-6748, 1089-7623. DOI: 10.1063/5.0040677. arXiv: 2102.08724[cond-mat]. URL: http://arxiv.org/abs/2102.08724.

[19] Lilo Höcker. "Building up a modular Na-K quantum gas experiment." PhD thesis. Heidelberg: Ruprecht-Karls-Universität, 2019.

[20] Lilo Höcker. "Progress and Challenges in Setting up an Ultracold 23Na-39K Quantum Gas Experiment." PhD thesis. 2024.

[21] W. Ketterle, D. Durfee, and D. Stamper-Kurn. "Making, probing and understanding Bose-Einstein condensates." In: *arXiv: Condensed Matter* (Apr. 2, 1999). URL: https://www.semanticscholar.org/paper/Making%2C-probing-and-understanding-Bose-Einstein-Ketterle-Durfee/9f009eaa3f252d14e744c3b94432cab2462e0306.

[22] Wolfgang Ketterle, Kendall B. Davis, Michael A. Joffe, Alex Martin, and David E. Pritchard. "High densities of cold atoms in a dark spontaneous-force optical trap." In: *Physical Review Letters* 70.15 (Apr. 12, 1993). Publisher: American Physical Society, pp. 2253–2256. DOI: 10.1103/PhysRevLett.70.2253. URL: https://link.aps.org/doi/10.1103/PhysRevLett.70.2253.

[23] Jan Kilinc. "Starting a Na-K experiment for simulating quantum many-body phenomena." Master Thesis. Heidelberg: Ruprecht-Karls-Universität, 2019.

[24] Jan Kilinc. "A new setup for experiments with an ultracold 23Na-39K mixture." In: (2024). Publisher: Heidelberg University Library. DOI: 10.11588/HEIDOK.00034438. URL: https://archiv.ub.uni-heidelberg.de/volltextserver/id/eprint/34438.

[25] G. Lamporesi, S. Donadello, S. Serafini, and G. Ferrari. "A compact high-flux source of cold sodium atoms." In: *Review of Scientific Instruments* 84.6 (), p. 063102. ISSN: 0034-6748, 1089-7623. DOI: 10.1063/1.4808375. arXiv: 1301.6566[cond-mat,physics:physics]. URL: http://arxiv.org/abs/1301.6566.

[26] Giacomo Lamporesi. *Two-component spin mixtures*. May 31, 2023. DOI: 10.48550/arXiv.2304.03711. arXiv: 2304.03711[cond-mat]. URL: http://arxiv.org/abs/2304.03711.

[27] Maciej Lewenstein, Anna Sanpera, Veronica Ahufinger, Bogdan Damski, Aditi Sen De, and Ujjwal Sen. "Ultracold atomic gases in optical lattices: mimicking condensed matter physics and beyond." In: *Advances in Physics* 56.2 (Mar. 2007), pp. 243–379. ISSN: 0001-8732, 1460-6976. DOI: 10.1080/00018730701223200. arXiv: cond-mat/0606771. URL: http://arxiv.org/abs/cond-mat/0606771.

[28] Harold J. Metcalf and Peter Van Der Straten. *Laser Cooling and Trapping*. Red. by R. Stephen Berry, Joseph L. Birman, Jeffrey W. Lynn, Mark P. Silverman, H. Eugene Stanley, and Mikhail Voloshin. Graduate Texts in Contemporary Physics. New York, NY: Springer, 1999. ISBN: 978-0-387-98728-6 978-1-4612-1470-0. DOI: 10.1007/978-1-4612-1470-0. URL: http://link.springer.com/10.1007/978-1-4612-1470-0.

[29] Florian Volker Nicolai. "Design and construction of a fiber-coupled tapered amplifier system." PhD thesis. Heidelberg: Ruprecht-Karls-Universität, 2017.

[30] C. J. Pethick and H. Smith. *Bose–Einstein Condensation in Dilute Gases*. 2nd ed. Cambridge: Cambridge University Press, 2008. ISBN: 978-0-521-84651-6. DOI: 10.1017/CBO9780511802850. URL: https://www.cambridge.org/core/books/boseeinstein-condensation-in-dilute-gases/CC439EAD70D78E47E9AF536DA7B203EC.

[31] Lev P. Pitaevskii, Sandro Stringari, Lev P. Pitaevskii, and Sandro Stringari. *Bose-Einstein Condensation*. International Series of Monographs on Physics. Oxford, New York: Oxford University Press, Apr. 3, 2003. 394 pp. ISBN: 978-0-19-850719-2.

[32] Lew Petrowitsch Pitaevskii. "Vortex Lines in an Imperfect Bose Gas." In: *Journal of Experimental and Theoretical Physics* 13 (1961), pp. 451–454.

[33] M. Prentiss, A. Cable, J. E. Bjorkholm, Steven Chu, E. L. Raab, and D. E. Pritchard. "Atomic-density-dependent losses in an optical trap." In: *Optics Letters* 13.6 (June 1, 1988). Publisher: Optica Publishing Group, pp. 452–454. ISSN: 1539-4794. DOI: 10.1364/OL.13.000452. URL: https://opg.optica.org/ol/abstract.cfm?uri=ol-13-6-452.

[34] Daryl W. Preston. "Doppler-free saturated absorption: Laser spectroscopy." In: *American Journal of Physics* 64.11 (Nov. 1, 1996), pp. 1432–1436. ISSN: 0002-9505. DOI: 10.1119/1.18457. URL: https://doi.org/10.1119/1.18457.

[35] E. L. Raab, M. Prentiss, Alex Cable, Steven Chu, and D. E. Pritchard. "Trapping of Neutral Sodium Atoms with Radiation Pressure." In: *Physical Review Letters* 59.23 (Dec. 7, 1987), pp. 2631–2634. ISSN: 0031-9007. DOI: 10.1103/PhysRevLett.59.2631. URL: https://link.aps.org/doi/10.1103/PhysRevLett.59.2631.

[36] M. S. Santos, P. Nussenzveig, A. Antunes, P. S. P. Cardona, and V. S. Bagnato. "Hyperfine-changing collision measurements in trap loss for mixed species in a magneto-optical trap." In: *Physical Review A* 60.5 (Nov. 1, 1999). Publisher: American Physical Society, pp. 3892–3895. DOI: 10.1103/PhysRevA.60.3892. URL: https://link.aps.org/doi/10.1103/PhysRevA.60.3892.

[37] Florian Schreck. *Lecture on Ultracold quantum gases*. URL: https://www.strontiumbec.com/Teaching/BEC/BEC_Lecture_UvA_FS_2021.pdf.

[38] Torben A. Schulze, Torsten Hartmann, Kai K. Voges, Matthias W. Gempel, Eberhard Tiemann, Alessandro Zenesini, and Silke Ospelkaus. “Feshbach spectroscopy and dual-species Bose-Einstein condensation of $^{23}\mathrm{Na}\text{\ensuremath{-}}^{39}\mathrm{K}$ mixtures.” In: *Physical Review A* 97.2 (Feb. 13, 2018). Publisher: American Physical Society, p. 023623. DOI: 10.1103/PhysRevA.97.023623. URL: https://link.aps.org/doi/10.1103/PhysRevA.97.023623.

[39] Vijay Pal Singh, Luigi Amico, and Ludwig Mathey. “Thermal suppression of demixing dynamics in a binary condensate.” In: *Physical Review Research* 5.4 (Oct. 13, 2023), p. 043042. ISSN: 2643-1564. DOI: 10.1103/PhysRevResearch.5.043042. URL: https://link.aps.org/doi/10.1103/PhysRevResearch.5.043042.

[40] Nicolas Spethmann, Farina Kindermann, Shincy John, Claudia Weber, Dieter Meschede, and Artur Widera. “Dynamics of Single Neutral Impurity Atoms Immersed in an Ultracold Gas.” In: *Physical Review Letters* 109.23 (Dec. 4, 2012). Publisher: American Physical Society, p. 235301. DOI: 10.1103/PhysRevLett.109.235301. URL: https://link.aps.org/doi/10.1103/PhysRevLett.109.235301.

[41] Daniel A Steck. “Quantum and Atom Optics.” In: ().

[42] Daniel A Steck. “Sodium D Line Data.” In: (2003).

[43] T. G. Tiecke. “Properties of Potassium.” In: (2019).

[44] T. G. Tiecke, S. D. Gensemer, A. Ludewig, and J. T. M. Walraven. “High-flux two-dimensional magneto-optical-trap source for cold lithium atoms.” In: *Physical Review A* 80.1 (July 20, 2009). Publisher: American Physical Society, p. 013409. DOI: 10.1103/PhysRevA.80.013409. URL: https://link.aps.org/doi/10.1103/PhysRevA.80.013409.

[45] E. Timmermans. “Phase Separation of Bose-Einstein Condensates.” In: *Physical Review Letters* 81.26 (Dec. 28, 1998). Publisher: American Physical Society, pp. 5718–5721. DOI: 10.1103/PhysRevLett.81.5718. URL: https://link.aps.org/doi/10.1103/PhysRevLett.81.5718.

[46] Marek Trippenbach, Krzysztof Góral, Kazimierz Rzazewski, Boris Malomed, and Y. B. Band. “Structure of binary Bose-Einstein condensates.” In: *Journal of Physics B: Atomic, Molecular and Optical Physics* 33.19 (Oct. 2000), p. 4017. ISSN: 0953-4075. DOI: 10.1088/0953-4075/33/19/314. URL: https://dx.doi.org/10.1088/0953-4075/33/19/314.

[47] Celia Viermann. “Cosmological particle production and curved spaces in an ultracold quantum gas.” PhD thesis.

[48] Celia Viermann et al. “Quantum field simulator for dynamics in curved spacetime.” In: *Nature* 611.7935 (Nov. 2022). Publisher: Nature Publishing Group, pp. 260–264. ISSN: 1476-4687. DOI: `10.1038/s41586-022-05313-9`. URL: `https://www.nature.com/articles/s41586-022-05313-9`.

[49] Andrejs Vorozcovs, Matthew Weel, Scott Beattie, Saviour Cauchi, and A. Kumarakrishnan. “Measurements of temperature scaling laws in an optically dense magneto-optical trap.” In: *JOSA B* 22.5 (May 1, 2005). Publisher: Optica Publishing Group, pp. 943–950. ISSN: 1520-8540. DOI: `10.1364/JOSAB.22.000943`. URL: `https://opg.optica.org/josab/abstract.cfm?uri=josab-22-5-943`.

[50] Tino Weber, Jens Herbig, Michael Mark, Hanns-Christoph Nägerl, and Rudolf Grimm. “Bose-Einstein Condensation of Cesium.” In: *Science* 299.5604 (Jan. 10, 2003). Publisher: American Association for the Advancement of Science, pp. 232–235. DOI: `10.1126/science.1079699`. URL: `https://www.science.org/doi/10.1126/science.1079699`.

[51] M. Weidemüller, T. Esslinger, M. A. Ol’shanii, A. Hemmerich, and T. W. Hänsch. “A Novel Scheme for Efficient Cooling below the Photon Recoil Limit.” In: *Europhysics Letters* 27.2 (July 1994), p. 109. ISSN: 0295-5075. DOI: `10.1209/0295-5075/27/2/006`. URL: `https://dx.doi.org/10.1209/0295-5075/27/2/006`.

[52] A. Weis and S. Derler. “Doppler modulation and Zeeman modulation: laser frequency stabilization without direct frequency modulation.” In: *Applied Optics* 27.13 (July 1, 1988). Publisher: Optica Publishing Group, pp. 2662–2665. ISSN: 2155-3165. DOI: `10.1364/AO.27.002662`. URL: `https://opg.optica.org/ao/abstract.cfm?uri=ao-27-13-2662`.

ACKNOWLEDGMENTS

I would like to sincerely thank everyone involved with the SoPa experiment over the last year, especially Lilo, Jan, Brian and Malaika who, through many fruitful discussions, managed to teach me everything I needed to know about the experiment to write this thesis while also being great colleagues. I also want to thank Helmut for all his helpful explanations about various physical and technical topics and for always being there to help when things go wrong. Furthermore, I want to thank everyone working on Markus' other experiments and the people from Thomas Gasenzers group for the lighthearted lunch breaks and generally good vibes during and outside of work. Lastly, I want to thank Markus Oberthaler, who made all of this possible, for always offering his advice and expertise on important topics like the overall strategy of the experiment and for generally being quite enjoyable to work with.

I also want to mention some of the tools I found quite useful while writing this thesis: For most schematics I used Inkscape, together with the Inkscape *ComponentLibrary* created by Alexander Franzen (`http://www.gwoptics.org/ComponentLibrary/`). It's licensed under the Creative Commons Attribution-NonCommercial 3.0 License.
This document was made using the *Classicthesis Typographic Thesis LaTeX template* created by André Miede, which is licensed under GNU General Public License (v2).

ERKLÄRUNG

Ich versichere, dass ich diese Arbeit selbstständig verfasst und keine anderen als die angegebenen Quellen und Hilfsmittel benutzt habe.

Heidelberg, den August 7, 2024

Anton Eberhardt